PROBLEMS AND INFORMATICS-AIDED SOLUTIONS IN RESEARCH OF NEURODEGENERATION WITH AN EMPHASIS ON QUANTITATIVE MORPHOLOGY

Ph.D. Thesis by

Tamás Ferenc Polgár

Supervised by:

Bernát Nógrádi, M.D., Ph.D.

Roland Patai, Ph.D.

Laboratory of Neuronal Plasticity, Molecular Neurobiology Research Unit,

Institute of Biophysics, Biological Research Centre, Szeged, Hungary

Doctoral School of Experimental and Preventive Medicine, University of Szeged, Szeged, Hungary

Neuroscience Research Group, Department of Neurology, University of Szeged, Szeged, Hungary

Szeged

2025

“Nevertheless, it is important to highlight that not a single brain disease can be fully understood, diagnosed, or treated, without deciphering the role played by microglia in it.”

Amanda Sierra et al. Cien Años de Microglía

List of publications

Publications providing the basis of the thesis

I. Nógrádi, B.*, **Polgár, T.F.***, Meszlényi, V., Kádár, Z., Hertelendy, P., Csáti, A., Szpisjak, L., Halmi, D., Erdélyi-Furka, B., Tóth, M., Molnár, F., Tóth, D., Bősze, Z., Boda, K., Klivényi, P., Siklós L., Patai R.. ChatGPT MD: is there any room for generative AI in neurology? *Plos One*, 19: e0310028, **2024** (IF (2024): 2.6, Journal Ranking: Q1)
*Equal contributors.

II. **Polgár, T.F**, Meszlényi, V., Nógrádi B., Körmöczy, L., Spisák, K., Tripolszki K., Széll, M., Obál I., Engelhardt, J.I., Siklós, L., Patai R.. Passive transfer of blood sera from ALS patients with identified mutations results in elevated motoneuronal calcium level and loss of motor neurons in the spinal cord of mice. *International Journal of Molecular Sciences*, 22: 9994, **2021** (IF (2021): 4.556, Journal Ranking: D1)

III. **Polgár, T.F.**, Spisák, K., Kádár, Z., Alodah, N., Szebeni, G.J., Klein, K., Patai, R., Siklós, L., Nógrádi, B. Photobleaching alters the morphometric analysis of fluorescently labeled neurons and microglial cells. *Pathology & Oncology Research*, 31: 1612087, **2025** (IF (2025): 2.3, Journal Ranking: Q2)

Manuscripts in preparation

I. **Polgár, T.F.**, Nógrádi, B., Kádár, Z., Siklós L., Klivényi, P. Artificial intelligence-aided assessment of inflammatory alterations in murine models of amyotrophic lateral sclerosis. *In preparation.*

Publications not included in the thesis

I. Dobra, G., Gyukity-Sebestyén, E., Bukva, M., Böröczky, T., Nyiraty, S., Bordacs, B., Várkonyi, T., Kocsis, A., Szabó, Z., Kecskeméti, G., **Polgár, T. F.**, Széll, M., & Búzás, K. Proteomic profiling of serum small extracellular vesicles predicts post-COVID syndrome development. *Clinical immunology*, 278: 110532, **2025** (IF: 4.5, Journal Ranking: Q2)

II. Ashfaq, R., Tóth, N., Kovács, A., Berkó, S., Katona, G., Ambrus, R., **Polgár, T. F.**, Szécsényi, M., Burián, K., & Budai-Szűcs, M. Hydrogel-Nanolipid Formulations for the Complex Anti-Inflammatory and Antimicrobial Therapy of Periodontitis. *Pharmaceutics*, 17(5): 620, **2025** (IF: 5.5, Journal Ranking: D1)

III. Shaikh, K. M., Walker, C. E., Tóth, D., Kuntam, S., **Polgár, T. F.**, Petrova, N. Z., Garland, H., Mackinder, L. C. M., Tóth, S. Z., & Spetea, C.:. The thylakoid- and pyrenoid-localized phosphate transporter PHT4-9 is essential for photosynthesis in Chlamydomonas. *Plant Physiology*, kiaf158, **2025** (IF: 6.5, Journal Ranking: D1)

IV. Mészáros, M., Phan, T.H.M., Vigh, J.P., Porkoláb, G., Kocsis, A., Szecskó, A., Páli, K. E., Cser, N. M., **Polgár, T.F.**, Kecskeméti, G., Walter, R.F., Schwamborn, C. J., Janáky, T., Jan, J., Veszelka, Sz. and Deli, M. A.: Alanine and glutathione targeting of dopamine- or ibuprofen-coupled polypeptide nanocarriers increases both crossing and protective effects on a blood–brain barrier model. *Fluids Barriers CNS*, 22: 18, **2025** (IF: 5.9, Journal Ranking:)

V. Szögi, T., Borsos, B. N., Masic, D., Radics, B., Bella, Z., Bánfi, A., Ördög, N., Zsiros, C., Kiricsi, Á., Pankotai-Bodó, G., Kovács, Á., Paróczai, D., Botkáné, A. L., Kajtár, B., Sükösd, F., Lehoczki, A., **Polgár, T.F.**, Letoha, A., Pankotai, T., & Tiszlavicz, L. Novel biomarkers of mitochondrial dysfunction in Long COVID patients. *GeroScience*, 47(2): 2245-2261, **2024** (IF: 5.3, Journal Ranking: D1)

VI. Koncz, M., Stirling, T., Hadj Mehdi, H., Méhi, O., Eszenyi, B., Asbóth, A., Apjok, G., Tóth, Á., Orosz, L., Vásárhelyi, B. M., Ari, E., Daruka, L., **Polgár, T. F.**, Schneider, G., Zalokh, S. A., Számel, M., Fekete, G., Bohár, B., Nagy Varga, K., Visnyovszki, Á., … Kintses, B.: Genomic surveillance as a scalable framework for precision phage therapy against antibiotic-resistant pathogens. *Cell*, 187(21): 5901-5918, **2024** (IF: 45.5, Journal Ranking: D1)

VII. Farkas, D., Szikora, S., Jijumon, A. S., **Polgár, T. F.**, Patai, R., Tóth, M. Á., Bugyi, B., Gajdos, T., Bíró, P., Novák, T., Erdélyi, M., & Mihály, J.: Peripheral thickening of the sarcomeres and pointed end elongation of the thin filaments are both promoted by SALS and its formin interaction partners. *PLoS genetics*, 20(1): e1011117, **2024** (IF: 4.5, Journal Ranking: D1)

VIII. Devadasu E., Kanna S.D., Neelam S., Yadav R.M., Nama S., Akhtar P., **Polgár T.F.**, Ughy B., Garab G., Lambrev P.H., Subramanyam R.: Long- and short-term acclimation of the photosynthetic apparatus to salinity in Chlamydomonas reinhardtii. The role of Stt7 protein kinase. *Frontiers in Plant Science*, 14: 051711, **2023** (IF: 6.627, Journal Ranking: Q1)

IX. Mészáros M., Phan T.H.M., Vigh J.P., Porkoláb G., Kocsis A., Páli E.K., **Polgár T.F.**, Walter F.R., Bolognin S., Schwamborn J.C., Jan J.S., Deli M.A., Veszelka S.: Targeting Human Endothelial Cells with Glutathione and Alanine Increases the Crossing of a Polypeptide Nanocarrier through a Blood-Brain Barrier Model and Entry to Human Brain Organoids. *Cells*, 12(3): 503, **2023** (IF: 7.666, Journal Ranking: Q1)

X. Hudák A., Morgan G., Bacovsky J., Patai R., **Polgár T.F.**, Letoha A., Pettko-Szandtner A., Vizler C., Szilák L., Letoha T.: Biodistribution and Cellular Internalization of Inactivated SARS-CoV-2 in Wild-Type Mice. *International Journal of Molecular Sciences*, 23(14): 7609, **2022** (IF: 6.208, Journal Ranking: D1)

XI. Veszelka Sz., Mészáros M., Porkoláb G., Szecskó A., Kondor N., Ferenc Gy., **Polgár T.F.**, Katona G., Kóta Z., Kelemen L., Páli T., Vigh J.P., Walter F.R., Bolognin S., Schwamborn J.C., Jan J., Deli M.A.: A Triple Combination of Targeting Ligands Increases the Penetration of Nanoparticles across a Blood-Brain Barrier Culture Model. *Pharmaceutics*, 14(1): 86, **2022** (IF: 6.321, Journal Ranking: Q1)

XII. Kartali T., Nyilasi I., Kocsubé S., Patai R., **Polgár T.F.**, Zsindely N., Nagy G., Bodai L., Lipinszki Z., Vágvölgyi Cs., Papp T.: Characterization of Four Novel dsRNA Viruses Isolated from Mucor hiemalis Strains. *Viruses*, 13(11): 2319, **2021** (IF: 5.048, Journal Ranking: Q1)

XIII. Koderi V. S., Shetty P., Deim Z., Terhes G., Urbán E., Váczi S., Patai R., Polgár T.F., Pertics B. Zs., Schneider Gy., Kovács T., Rákhely G.: Survival Comes at a Cost : A Coevolution of Phage and Its Host Leads to Phage Resistance and Antibiotic Sensitivity

of Pseudomonas aeruginosa Multidrug Resistant Strains. *Frontiers in Microbiology,* 12: 783722, **2021** (IF: 5.640, Journal Ranking: Q1)

XIV. Topal G. R., Mészáros M., Porkoláb G., Szecskó A., **Polgár T.F.**, Siklós L., Deli M. A., Veszelka Sz., Bozkir A.: ApoE-Targeting Increases the Transfer of Solid Lipid Nanoparticles with Donepezil Cargo across a Culture Model of the Blood–Brain Barrier. *Pharmaceutics*, 13(1): 38, **2020** (IF: 6.321, Journal Ranking: Q1)

XV. Papp A., Horváth T., Igaz N., Gopisetty M.K., Kiricsi M., Berkesi D.S., Kozma G., Kónya Z., Wilhelm I., Patai R., **Polgár T.F.**, Bellák T., Tiszlavicz L., Razga Z., Vezér T.: Presence of Titanium and Toxic Effects Observed in Rat Lungs, Kidneys, and Central Nervous System in vivo and in Cultured Astrocytes in vitro on Exposure by Titanium Dioxide Nanorods. *International Journal of Nanomedicine,* 15: 9939-9960, **2020** (IF: 5.93, Journal Ranking: D1)

XVI. Meszlényi V., Patai R., **Polgár T.F.**, Nógrádi B., Körmöczy L., Kristóf R., Spisák K., Tripolszki K., Széll M., Obál I., Engelhardt J.I., Siklós L.: Passive Transfer of Sera from ALS Patients with Identified Mutations Evokes an Increased Synaptic Vesicle Number and Elevation of Calcium Levels in Motor Axon Terminals, Similar to Sera from Sporadic Patients. *International Journal of Molecular Sciences,* 21(15): 5566, **2020** (IF: 5.294, Journal Ranking: D1)

XVII. Nógrádi B., Meszlényi V., Patai R., **Polgár T.F.**, Spisák K., Kristóf R., Siklós L.: Diazoxide blocks or reduces microgliosis when applied prior or subsequent to motor neuron injury in mice. *Brain Research,* 1741: 146875, **2020** (IF: 3.252, Journal Ranking: Q2)

XVIII. Zsiros O., Nagy G., Patai R., Solymosi K., Gasser U., **Polgár T.F.**, Garab G., Kovács L., Hörcsik Z.T.: Similarities and Differences in the Effects of Toxic Concentrations of Cadmium and Chromium on the Structure and Functions of Thylakoid Membranes in Chlorella variabilis. *Frontiers in Plant Science,* 11: 1006, **2020** (IF: 5.753, Journal Ranking: D1)

XIX. Kartali T., Nyilasi I., Szabó B., Kocsubé S., Patai R., **Polgár T.F.**, Nagy G., Vágvölgyi Cs., Papp T.: Detection and molecular characterization of novel dsRNA viruses related to the Totiviridae family in Umbelopsis ramanniana. *Frontiers in Cellular and Infection Microbiology*, 9: 249, **2019** (IF: 5.293, Journal Ranking: D1)

CONTENTS

List of abbreviations

A488	Alexa Fluor 488 Plus
A546	Alexa Fluor 546
AI	artificial intelligence
ALS	amyotrophic lateral sclerosis (ALS)
DAB	diaminobenzidine
EDD	electron-dense deposit
Iba1	ionized calcium-binding adaptor molecule 1
IF	immunofluorescence
MD	medical doctor
MN	motor neuron
ns	non-significant
PBS	phosphate buffered saline
PFA	paraformaldehyde
SOD1	superoxide dismutase
TPBS	PBS containing 0.2 % Triton X-100

Introduction

The healthy human brain contains approximately 86 billion neurons and 40-130 billion glial cells [1]. Counting neuronal and non-neuronal cells in the anatomic regions of interest is one of the most basic (and important) techniques in studies investigating the morphological alterations in pathological conditions of the nervous system. The estimated number of brain cells changed robustly over more than 150 years of cell counting [1], but it is certain that their number and morphology change in almost any neuronal disease [2] and even in healthy ageing [3]. Therefore, the use of accurate methods to characterize number and morphological changes might be essential in understanding pathological processes, which is the first step in a lengthy course of investigations to develop treatments to slow disease progression and ultimately cure the patients.

The type of neurons affected depends on the disease itself – for instance, in the case of amyotrophic lateral sclerosis (ALS), the motor neurons (MNs) in the motor cortex and in the spinal cord are impacted by the degenerative processes [4]. Thus, before counting or characterizing the morphology of cells, first, a hierarchic sampling paradigm must be established, specifying tissue type, anatomical regions of interest, sub-regions, etc. [5,6] (Figure 1).

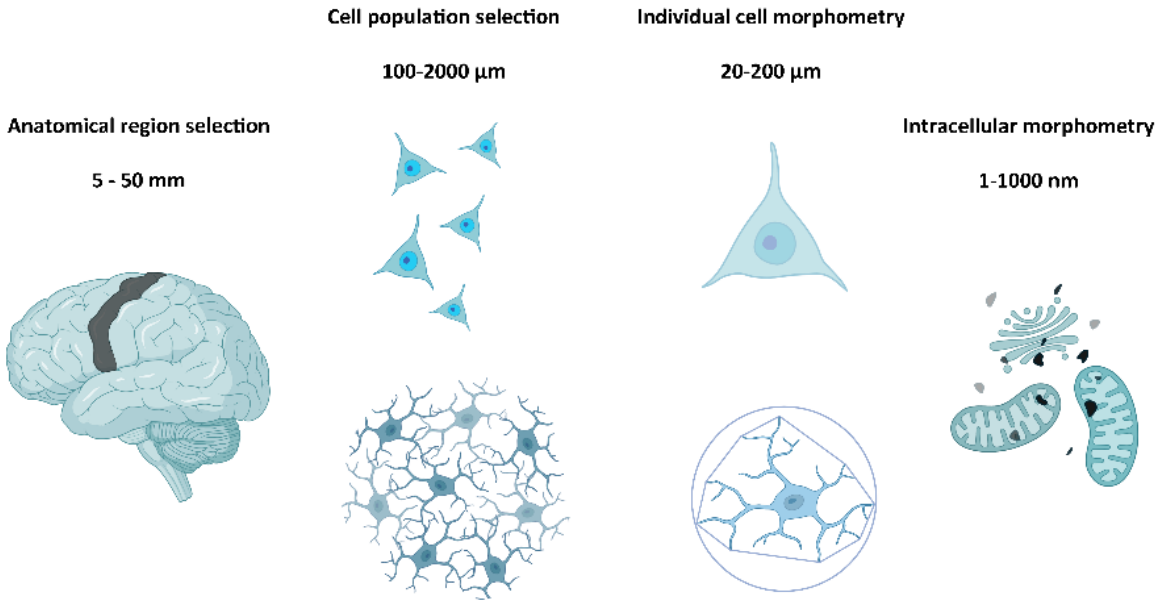

Figure 1. *Scheme of hierarchic sampling for morphological characterization of neural and microglial cells at light (anatomical region, cell populations and individual cells) and electron microscopic (intracellular components) level.*

Then, finding a correct method to count cells, however, is not trivial. Despite the increasing application of 3D microscopy, based on tissue clearing techniques which enable the visualization and characterization of volumetric objects as a whole [7], most morphometric works in biology/pathology are still based on conventional microscopy of thin sections (Figure 2).

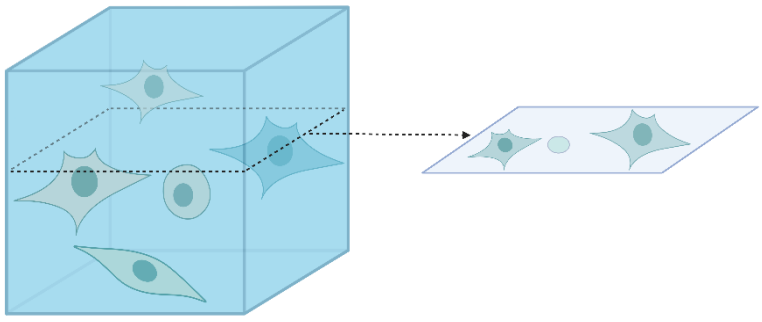

Figure 2. *While 3D microscopy allows the observation and characterization of entire cells, in section-based conventional microscopy only cross sections of the cells are visible.*

The problem stems from that based on practically two-dimensional measurements (e.g., area, length of line, etc.), made in thin sections, three-dimensional data (e.g., number / volume, surface area, etc.) have to be derived, possibly with assumption-free, or unbiased methods [8, 9]. To satisfy this, as a rule of thumb, the arithmetical sum of the dimension of a component to be investigated, such as volume (V, 3-D), surface (S, 2-D), length (L, 1-D), and number (N, 0-D), and the dimension of the appropriate probe, i.e., point (p, 0-D), line (l, 1-D), area (a, 2-D), volume (v, 3-D), respectively, has the be uniformly three [10, 6]. Thus, to determine volumetric parameters, i.e. number of cells / volumes, 3-D probes have to be applied. The specific method, however, must be individually developed, optimized to the investigated problem, which, in our case, is the study of motoneuronal and calcium homeostatic alterations in a model of ALS.

More than a decade ago, since the recognition that in the process of neurodegenerative diseases the salient victims of the disease, i.e., the neurons, are not the lone cellular players, the role of neighboring astrocytes and microglial cells became evident [11, 12]. Particularly, in ALS, which is in the focus of our research, Dr. Appel, in an article in tribute of V. Arkansas and K. Engel – pioneers of understanding mechanisms underlying neuromuscular diseases – reviewed this fact in such a way that in ALS, neurons do not die by themselves but as a consequence of an interaction between MNs and microglial cells [13]. Thus, since immunofluorescence (IF) microscopy has the advantage of multiple staining and simultaneous visualization of different cells and cellular compartments [14], it is not surprising that it became widely used in research of cellular interactions in neurodegenerative processes. Parallel to that the IF microscopy became broadly used, the need to consider the quantitative aspects of the method emerged [15]. In such experiments, the amount and distribution of specific cellular components are aimed to be determined based on the strength of the emitted fluorescent signal. However, such quantitative evaluation is rather challenging due to photobleaching, which is a well-known phenomenon that occurs when fluorophores lose their ability to emit fluorescence upon prolonged exposure to excitation light. Photobleaching is primarily attributed to the irreversible damage and chemical alterations incurred by fluorophores when subjected to high-energy excitation light [16,17]. This weakening in fluorescence may particularly affect the morphological characterization of objects with fine process arborization, for example, microglia and astrocytes. As the fluorescent signal is fading over illumination time and

eventually disappears, this may alter not only the number of recognized cells, obtained by quantitative data after image analysis [16], but also the fractal parameters describing the arborization of these cells, which, otherwise, can quickly remodel [18] as a reaction to local pathological changes [19]. The magnitude of the effect of photobleaching on quantitative morphometric parameters of fluorescently labelled cells, however, is not known in detail.

The goal of experimental neurology research is to better understand the pathomechanisms underlying human neurodegenerative diseases, to slow down or eventually halt disease progression. Since human brain samples, due to ethical considerations, are only available for direct examination in exceptional cases, experimental models mimicking certain aspects of the investigated disease are utilized. The usefulness of the animal models in understanding pathological changes in the diseased central nervous system is exemplified by the case of amyotrophic lateral sclerosis. In ALS, a part of the diseased MN, the motor nerve terminal, is available for direct microscopic, histochemical, and pathological examinations after a small surgery called muscle biopsy [20]. In such a study, Siklós described pathological alterations (swelling) of mitochondria and an increase of intracellular and intramitochondrial calcium within the axon terminals [21]. As transgenic mice, which developed pathological changes that resembled those in human ALS became available [22], after similar examinations, analogous alterations could be detected in their motor axon terminals as in those of the patients [23]. Since the spinal cord and brain samples of these animals could be similarly characterized, the observations in these regions of the central nervous system enabled the extrapolations to the human central nervous system.

The utility of animal models of neurodegenerative diseases is not limited to the availability of the entire nervous system for different types of examinations but also provides a shorter duration for the development of the disease and the possibility of introducing and testing potential medical treatments. In human neurodegenerative diseases, however, any potential treatment is delayed by the relatively long diagnostic time. ALS has an exceptionally long diagnostic time (from symptom onset to confirmed diagnosis, the range is from half to one and a half years [24,25]), since the disease shows heterogeneous progression and symptoms, therefore, there is no single test for the disease. Thus, the diagnosis is based on a combination of inclusion and exclusion clinical criteria [26].

The question asked by Mitchell et al. in the title of their paper published in 2010, “Can we do better?” was also investigated in the thesis by showing a simple, AI-generated example of automatizing repetitive image analysis and evaluating the potential supporting role of artificial intelligence in setting up or facilitating diagnosis of neurodegenerative diseases.

Aims

Characterization of the motoneuronal calcium level and loss of motor neurons in a model of ALS using optimized dissector methods

Characterization of the effect of photobleaching on the morphometric analysis of fluorescently labeled cells in the central nervous system

Characterization of the potential of general artificial intelligence in image analysis and the diagnosis of neurological diseases

Material and methods

Ethical considerations

Regular animal housing

The protection and welfare of animals were carried out according to the national law (Edict 40/2013 (II.14)) which conforms to the European Union executory directive on the protection of animals used for scientific purposes (Directive 2010/63/EU amended by the Regulation (EU) 2019/1010).

Selection of patients and obtaining human blood samples

Ethical approvals for obtaining and storing blood samples for research purposes from ALS patients and healthy controls in an anonymous manner were given by The Human Investigation Review Board, University of Szeged, Hungary (#2557/2009). All experiments using human samples in our project agreed with the declaration of the Medical World Federation proclaimed in Helsinki 1964. All participants have given their informed, written consent to participate in this study.

Altogether 14 ALS patients and 3 age-matched healthy control individuals participated in the study. All the blood samples were stored at the Department of Neurology, University of Szeged in Szeged, Hungary. All patients satisfied the “probable” or “definite” El Escorial revisited criteria (1). Selection criteria also included the lack of known systemic autoimmune disorders.

Passive transfer of human sera to mice

Ethical approvals for the scientific experiments involving animals were given by The Government Office in Csongrád-Csanád County, Hungary (#XI/4962/2015; #XVI/819/2021) and by The Committee for Animal Experiments of the University of Szeged, Szeged, Hungary (XVI./2733/2022) and by the Ethical Committee for the protection of Animals in Scientific Research at the Biological Research Center, Szeged, Hungary (#XVI/819/2021). All efforts were made to minimize animal suffering throughout the experiments.

Forty-eight male Balb/c mice, obtained from Charles River Appoints AnimaLab Hungary Kft. (Vác, Hungary), were injected intraperitoneally each day with 1 ml serum from ALS patients (n=14) or healthy individuals (n=3) for two days. All animals received sera from the same

patient during the inoculation period. One group of animals did not receive any injection and was used as the untreated control (n=3).

During the two-day inoculation period, before sacrificing them, animals were housed in plastic cages (5 animals/cage, at most) in a thermoneutral environment (22±3 °C) and reversed 12 hours light/dark cycle with access to water and regular rodent chow ad libitum.

Testing the diagnostic potential of AI

Since all guidelines and regulations, particularly the General Data Protection Regulation are effective in Hungary, which prohibits the use of real patient data, therefore no sensitive medical information or patient data was utilized in conducting the study. Instead, synthetic data generated by neurological experts were employed, to portray the descriptive histories of patients diagnosed with neurology-related diseases. Thus, no informed consent was applicable.

Sample preparation methods

Preparation for light microscopic histology

Under irreversible anesthesia with Avertin (Merck, Darmstadt, Germany), the experimental mice were transcardially perfused with 10 mM phosphate buffered saline (PBS; pH 7.4) followed by 4% paraformaldehyde (PFA, Merck) fixation in 10 mM PBS (pH 7.4). The spinal cord samples were removed and were fixed overnight in 4% PFA. After fixation, segments from the intumescence of the lumbar spinal cords were spared for quantification of motoneuronal survival in the ventrolateral MN pools. As in our previous experiments, the lumbar section was chosen for evaluation since hindlimb weakness is one of the first symptoms of MN degeneration in immune-mediated and transgenic animal models [29,30]. Sections were placed in a 30% sucrose solution. After cryoprotection, consecutive 10 µm thin sections were cut with a cryostat (Reichert-Jung, Leica Biosystems, Wetzlar, Germany) and stained with cresyl violet.

Preparation for calcium histochemistry

Under irreversible anesthesia with Avertin (Merck, Darmstadt, Germany), the experimental mice were transcardially perfused with 10 mM phosphate buffered saline (PBS; pH 7.4), then the spinal cord samples were removed and prepared for electron microscopic analytical study for calcium, as described originally by Borgers and coworkers [31], which demonstrates tissue calcium as electron dense deposits (EDDs), see e.g., Patai et al. [32]. The method was adapted

and regularly tested for specificity for calcium in our laboratory. Furthermore, it provides good preservation of the tissue, suitable for electron microscopy and results in the formation of EDDs due to the precipitation of tissue calcium by the fixative [32–35]. Briefly: After fixation, specimens were then rinsed in 7.5% sucrose (Molar) containing 90 mM potassium oxalate (pH 7.4), postfixed with 2% potassium pyroantimonate (Merck) + 1% osmic acid (Sigma; pH adjusted to 7.4 with acetic acid (Molar)) for 2 h (4 °C). Next, specimens were rinsed in distilled water (pH adjusted to 10 with KOH) for 10 min, dehydrated in a graded series of ethanol (Molar), processed through propylene oxide (Sigma), and embedded in Durcupan ACM (Fluka). Blocks were polymerized for 48 h at 56 °C. Semithin (0.3 µm) sections were cut from the blocks on an Ultracut UCT ultramicrotome (Leica), to identify pools of MNs under a light microscope, then after trimming the blocks to the appropriate regions, ultrathin sections (60 nm) were cut, mounted on uncoated 300 mesh copper grids (Electron Microscopy Sciences) and contrasted with uranyl acetate and lead citrate.

Immunofluorescence labelling

Under irreversible anesthesia with Avertin (Merck, Darmstadt, Germany), mice were transcardially perfused with 10 mM phosphate buffered saline (PBS; pH 7.4) followed by 4% paraformaldehyde (Merck) fixation in 10 mM PBS (pH 7.4).The lumbar spinal cord was removed and fixed overnight in the same fixative at 4 °C. Then the samples were cryoprotected in 30% sucrose (Merck), dissolved in 10 mM PBS, for 1 day at 4 °C and embedded in optimal cutting temperature medium (Sakura Finetek, CA, USA). 30 µm thick consecutive sections were cut with a CM1860 cryostat (Leica, Wetzlar, Germany), and collected individually in 10 mM PBS in wells of tissue culture plates and stored at 4 °C until processed for free-floating immunohistochemical staining. Sections were rinsed with 10 mM PBS (three changes, 5 minutes each), then blocked with 3% normal donkey serum (Sigma, St. Louis, MO, USA; Cat# D9663, RRID: AB_2810235) in 10 mM PBS containing 0.2 % Triton X-100 (TPBS) for 60 min. Next, sections were incubated overnight at 4 °C with the primary antibody (Table 1), diluted in 3% normal donkey serum in 10 mM PBS.

Staining	Primary antibodies	Secondary antibodies
NeuN (IF)	Anti-NeuN polyclonal antibody, diluted to 1:500 (Merck, Cat# ABN78, RRID:AB_10807945)	Donkey anti-rabbit Alexa Fluor Plus 488 secondary antibody diluted to 1:500 (Invitrogen, Waltham, MA, USA; Cat# A32790, RRID:AB_2762823) Donkey anti-rabbit Alexa Fluor 546 secondary antibody diluted to 1:500 (Invitrogen, Cat# A11056; RRID:AB_2534103)
Iba1 (IF)	Anti-Iba1 polyclonal antibody, diluted to 1:1000 (Wako Chemicals, Neuss, Germany, Cat# 019-19741, RRID:AB_839504)	
ChAT (IF)	Anti-ChAT polyclonal antibody, diluted to 1:500 (Merck, Cat# AB144P, RRID:AB_2079751)	Donkey anti-sheep Alexa Fluor 488 secondary antibody diluted to 1:500 (Invitrogen, Cat# A11015; RRID:AB_141362)
Iba1 (DAB)	Anti-Iba1 polyclonal antibody, diluted to 1:250 (Wako Chemicals, Neuss, Germany, Cat# 019-19741, RRID:AB_839504)	Goat anti-rabbit biotinylated secondary antibody diluted to 1:500 (Vector Labs, Cat# BA-1000-1.5, RRID:AB_2313606)

Table 1. *List of primary and secondary antibodies used for immunostaining.*

Next day, sections were washed with 10 mM PBS (three changes, 5 minutes each), then incubated with donkey anti-rabbit Alexa Fluor 488 Plus (A488; Invitrogen, Waltham, MA, USA; Cat# A32790, RRID:AB_2762823) or Alexa Fluor 546 (A546; Invitrogen, Cat# A11056; RRID:AB_2534103) secondary antibody, diluted to 1:400 in 3% normal donkey serum and 10 mM PBS for 60 minutes at room temperature. Afterward, sections were washed in 10 mM PBS (three changes, 5 minutes each), mounted on silane-coated glass slides, and covered with Fluoromount-G mounting media (Invitrogen, Cat# 00-4958-02) to match the refractive index and to minimize the effect of photobleaching.

Combined fluorescent and DAB-based immunostaining

To compensate for the fading-induced signal loss at least in one of the labeled cell types, the conventional diaminobenzidine (DAB)-based and immunostaining was combined. Tissue samples were prepared for immunostaining as described previously. 30 µm-thick sections were

cut with a cryostat and collected in 10 mM PBS and stored at 4 °C until processed for free-floating combined staining. Sections were rinsed, blocked to reduce non-specific staining in the same way as it was done with the fluorescent method, with an additional step to block the endogenous peroxidase activity with 0.3% hydrogen peroxide in 10 mM TPBS. This was followed by overnight incubation at 4 °C with a primary antibody cocktail containing a polyclonal rabbit-anti-rat antibody against ionized calcium-binding adaptor molecule 1 (Iba1) and a polyclonal sheep-anti-ChAT antibody (Table 1) diluted to 1:250 and to 1:500, respectively, in 10 mM TPBS. After washing in 10 mM PBS (3 changes, 5 min each), sections were incubated at room temperature in a donkey-anti-sheep A488 fluorescent secondary antibodies for 1 hour, dissolved in 1:100 dilution in 10 mM TPBS. Afterwards, non-specific staining was blocked for 1 hour with a mixture of 1%-1% normal goat (Vector Laboratories) and normal donkey serum (Sigma) in 10 mM TPBS for 1 hour, then sections were incubated in a biotinylated goat-anti-rabbit antibody. Next, all the sections were rinsed in 10 mM PBS (3 changes, 5 min each), incubated in the avidin-biotin complex diluted to 1:1600 in PBS for 1 hour at room temperature. Next, after washing in 10 mM PBS, the reactions were visualized by incubation in 5% DAB in 10 mM PBS for 15 min. Finally, sections were washed in 10 mM PBS (3 changes, 5 min each), mounted on silane-coated glass slides, covered with Gel/Mount (Biomeda, Foster City, CA, USA) and visualized under a brightfield/fluorescent microscope.

Quantitative morphometry

Counting of lumbar MNs

Estimation of the number of MNs was performed using the optical dissector method on the cresyl-violet-stained samples. Images were recorded and examined with the Image-Pro Plus IPP image analysis program (Media Cybernetics) and a MicroPublisher 5.0 RTV charge-coupled device camera (QImaging) attached to an Eclipse 80i (Nikon) light microscope. The MNs were identified by their size, location in the ventrolateral position, and their ultrastructural features. The anatomical border of the ventrolateral pool of MNs was determined using the method described by Kong et al. [36]. The cells were counted if they met the selection criterion of the dissector based on the “thin focus microscopy” approach [8]. In our case MNs were counted if their nucleolus was visible in the lowest focal plane, called the reference plane, but not present in the uppermost focal plane, called the lookup plane. Counts from consecutive sections (n=8/animal) were pooled for animals, and the average numbers of MNs in the lumbar

segments were determined for each group. The counts were expressed N / mm^3, where the reference volume was determined by the section thickness and the boundary of the ventrolateral MN pool.

Quantification of the intracellular calcium

Sections were screened for the presence of the profiles of MNs in the ventral horns of the lumbar spinal cord, and images were recorded in a JEM-1400Flash transmission electron microscope (JEOL, Tokyo, Japan) until cytoplasm images from 15 MNs could be collected for microscopic analysis from every group. 16-bit grayscale images were recorded at an instrumental magnification of 12000× with a 2k×2k high-sensitivity scientific complementary metal-oxide-semiconductor camera (Matataki Flash sCMOS, JEOL) and saved in tagged image file format. As the unique, irregular shape, the electron density and the location of the EEDs make it impossible to form a rule-based decision system on pixel intensity or geometry, conventional digital image filtering does not have a toolset to automatically detect the deposits of interest. It seems possible to mix a conventional decision-making system with machine learning to determine the relative volume of the cytoplasm and mitochondria occupied by the EDDs representing the calcium precipitates, although it requires a training sample set so precise and enormous that our preliminary experiments (aiming to automatize this process) were unsuccessful. Thus, volume was determined manually by point counting methods [36,37], which was modified for these unique structures and photographic conditions [34] (Figure 3).

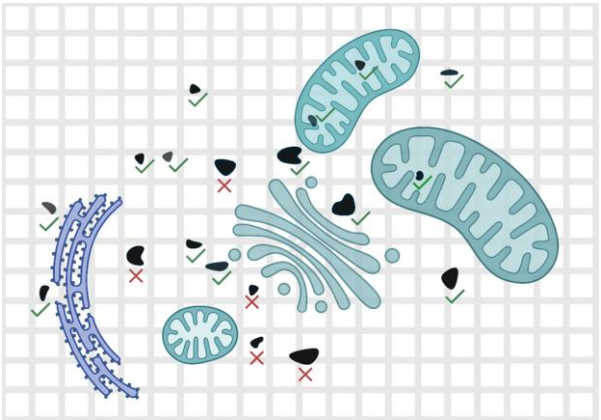

Figure 3. *Structures are marked positive if the point of interest (the electron-dense deposits representing the calcium precipitates in our case) overlaps the counting grid or the prolongation of the counting crosses.*

The recorded pictures were analyzed with the built-in modules of the Image-Pro Plus (Media Cybernetics; Rockville, MD, USA) image analysis software. The tessellation of sampling points was superimposed on each electron microscopic image, then sampling points hitting the cytoplasm in each image served as reference areas and were counted. Sampling points hitting the EDDs within the reference area were counted as well. The corresponding counts obtained in the individual fields were summed up throughout the series of the identified MN cytoplasm in each animal [38]. The appropriate ratios expressing the relative amount of EDDs within these structures were calculated for each animal.

Statistical analysis of calcium content and number of MNs

To determine the average volume occupied by EDDs within the cellular compartments of MNs, the data derived from individual electron microscopic fields were pooled according to animals and groups. 15-15 cytoplasmic areas of MNs were analyzed on the electron microscopic images from each animal. The number of MNs on both sides of the lumbar spinal cord was determined on cresyl violet stained samples (n=8/animal), and values were averaged per animal. Differences among multiple means of the volume density of the EDDs were assessed by the one-way analysis of variance, followed by the Bonferroni post-hoc test. Expectation-Maximization cluster analysis was performed with WEKA (version 3.8.3, Waikato, New Zealand) to investigate the cross-relation of the volume density of EDDs and the loss of MNs in ALS patients and controls.

Image analysis for measuring the effect of photobleaching

To avoid photobleaching before capturing the first image, a dedicated section on the slide served as a control to set the imaging parameters of the microscope and the Micropublisher 5.0 RTV camera (Teledyne QImaging, Surrey, Canada), then uniform image acquisition parameters (exposure time, acquisition gain, -gamma, -offset, -resolution) were used during capturing of time series. After setting the parameters, an area with uniformly distributed cells was selected, and the focus was briefly adjusted before capturing the first image. Then a single image was taken after 30, 60, 120, 300, 600, and 900 seconds of illumination to investigate the effect of fluorescent fading by measuring the following parameters: i) The mean pixel intensities of the whole microscopic images at different observation times and staining methods were measured

with the Histogram module of the Photoshop program (Adobe, San Jose, CA, USA). ii) Changes in the numbers of detectable NeuN-positive cell profiles were determined: Those cells which discernable nucleus were counted at each time point and compared to the cell counts obtained at the initial image. Those cells with no detectable nucleus after a certain illumination time were considered “faded”. iii) The value of pixels forming microglia/macrophage cell profiles was determined using an automated macro module developed in our laboratory for the Image-Pro Plus (Media Cybernetics, Rockville, MD, USA) image analysis software [39]. Relative differences in the values obtained at different observation times and staining methods were measured to express the effect of fluorescent fading using the background parameters obtained in the initial image. iv) Fractal geometrical parameters were measured according to the work of Fernández-Arjona and her colleagues [40]. Sections were screened under the microscope at 20× magnification with a Plan Fluor 20x/0.50 DIC N2 objective (Nikon). Microglial cells were identified and captured at different observation times and staining methods to visualize the complete arborization of the microglial processes. The semi-automated segmentation requires a certain amount of detail visibility. For this, an endpoint of detection was determined based on mean pixel intensity; cell profiles from A488 staining were segmented after 0 and 900 seconds of illumination, while cell profiles from A546 staining were segmented after 120 seconds of illumination. Individual cell profiles were segmented and converted to a binary image, then continuity errors were corrected using Photoshop (Adobe) and ImageJ (National Institute of Health, Bethesda, MA, USA). From the segmented microglia profiles, cell area, cell perimeter, fractal dimension, lacunarity, span ratio, density, and circularity were extracted by the Box Counting Fractal Analysis method using the FracLac plugin of ImageJ [41]. To further assess the effect of photobleaching on microglia population parameters, we used ImageJ’s area fraction attribute.

ImageJ is widely used by biologists and medical doctors for image processing and morphometry due to its availability and usability without any experience in programming. While such experience is not necessarily required, the manual image analysis processes can be slow and repetitive (e.g. separating channels, projecting z-stacks, filtering, color thresholding, segmenting, and measuring). To emulate an experienced biologist without previous programming knowledge, we used ChatGPT to generate a macro (“write me a simple macro”) integrated into ImageJ to help segmenting the microglia population, specifying the environment

("using ImageJ, Python 2/Jython"), the interface ("showing a window with an open file button"), and the behavior ("by clicking on the button, a regular file opener opens, listing .tif files. By opening the selected file, the macro converts it to grayscale and opens the threshold window with "triangle" settings. When the button is clicked again, before performing the steps above, the macro closes all opened windows") (Supplementary File 1.).

Testing diagnostic potential of AI in neurological diseases

Data generation

Synthetic cases with patient history and a brief, focused neurological status (n = 200) were generated by neurological experts (n = 5) and structured into a lifelike free-text form without abbreviations. The following guidelines were used for the synthetic case generation: a) patient history had to include leading symptoms, the onset, and characteristics of the symptoms; b) any previous major diseases or drugs had to be outlined in the patient history; c) the neurological status had to include any alteration compared to a "negative" status; d) the cases had to be realistic (i.e., on most occasions, the expert who generated the case has previously encountered a similar real-life scenario); and e) representative in terms of distribution (i.e., fewer cases were generated to represent rare disorders). While most of the cases represent the typical clinical appearance of a disorder, cases with atypical representations of a disease were not excluded. The synthetic cases represented real-life scenarios and a wide range of neurological diseases, varying from the most common cases to rare ones (Table 2).

Major disease groups (n=200)	
Neurovascular diseases	n=43
Neuroinfectious diseases	n=7
Neuromuscular and peripheral nerve disorders	n=23
Neurodegenerative disorders	n=24
Demyelination disorders of the CNS	n=10
Metabolic disorders	n=7
Headache syndromes	n=14
Spinal cord and radicular syndromes	n=8
Neurooncological disorders	n=11
Epilepsy and seizures	n=8
Hereditary neurological disorders	n=17
Other disorders	n=28

Table 2. *Classification of disease subgroups.*

Generation of the AI-given diagnoses

The synthetic cases (n = 200) were fed into ChatGPT (developed by OpenAI (https://openai.com/), accessed between February 8–17, 2023). We asked the large language model to list the top five most probable diagnoses in decreasing order of probability, then we created three groups that represented the most probable diagnosis (ChatGPT Top1), the three most likely (ChatGPT Top3), and the five most likely diagnosis (ChatGPT Top5). In certain cases, the task of giving the five most probable diagnoses was forced on the AI; however, the answer of ChatGPT stated that the most probable diagnosis is the correct one with maximum certainty. For this purpose, numerous feeding prompts have been tried, and prompt engineering revealed that the best and clearest way to feed our data is to ask: "Give us the five most probable diagnoses for the following case with decreasing order of probability:" followed by the brief history and anamneses.

Statistical analysis of motor neuron loss and calcium levels in the ALS serum transfer experiments

To determine the average volume occupied by EDDs within the cellular compartments of MNs, the data derived from individual electron microscopic fields were pooled according to animals and passive transfer groups. From each animal, 15-15 perikaryal areas were analyzed on the electron microscopic images of these MNs. The number of MNs on both sides of the lumbar

spinal cord was determined on cresyl-violet-stained samples (n=8/animal), and values were averaged per animal. Differences among multiple means of the volume density of the EDDs were assessed by the one-way analysis of variance, followed by the Bonferroni post hoc test. Expectation–Maximization cluster analysis was performed with WEKA (version 3.8.3, Waikato, New Zealand) to investigate the cross-relation of the volume density of EDDs and the loss of MNs in patients with different ALS genotypes and controls. All statistical analyses were performed with R (version 3.6.2, R Foundation for Statistical Computing, Vienna, Austria) with R Studio Integrated Development Environment (version 1.1.453, RStudio Inc., Boston, MA, USA) for Windows. Data are presented as mean values ± the standard error of the means (s.e.m.).

Statistical analysis of the experiments on photobleaching

To determine the average intensity loss, the number of NeuN-positive neurons and the relative changes in the microglial area 15-15 sections were imaged from 0 s to 900 s of illumination. Altogether 90 individual profiles, two from each image, were selected and segmented from these sections (n = 15/group) and were pooled according to the fluorophore and illumination time. To measure the effect of fading during the illumination, linear regression was also conducted using the stats statistical package in Python (version 3.10.9, python.org) on signal intensity loss measurements. Before each comparison, Shapiro-Wilk normality test was used, followed by the appropriate parametric/non-parametric statistical test to assess the differences among multiple means of intensity loss, the number of neurons, relative changes of microglial coverage and changes in the fractal parameters. In each case, the statistical test is specified in the figure legends. Data are presented as mean values ± the standard error of the means (s.e.m.). The statistical analyses were performed in Prism (version 8.0.1.244, GraphPad Software, San Diego, CA, United States).

Statistical analysis of the experiments on diagnostic accuracy of ChatGPT

PS Power and Sample Size software (Department of Biostatistics, Vanderbilt University Nashville, TN, USA) was used to determine the appropriate number of participants in the study to achieve feasible statistical power with the given intergroup differences and standard deviations. Comparison of the ratios of successful diagnosis by medical doctors (MDs), experts, and ChatGPT was performed using the Generalized Estimating Equations procedure of SPSS

version 29.0 (IBM; Armonk, New York, USA). This method takes into consideration that measurements are not independent because each participant decided on the same diagnosis. The dependent variable was 0 or 1 according to success or failure to give an appropriate diagnosis, independent variables were the participants and groups (MDs, Experts, ChatGPT Top1, ChatGPT Top3, ChatGPT Top5), for the model binomial distribution with logit link function was used with exchangeable working correlation matrix. Pairwise comparisons of group means, expressed as percentage ± standard error, were based on estimated marginal means with Sidak adjustment for multiple comparisons. Wald large-sample interval estimation for proportions was used to find binomial confidence intervals (CI95) and expressed as CI95% lower value - CI95% upper value.

Results

Effect of passive transfer of ALS sera on survival of MNs and intracellular calcium

Loss of lumbar MNs in mice after injection of ALS sera

Considering the probable instability in the results of neuronal cell number counting using immunofluorescence, a cresyl-violet staining was used to determine MN loss. This staining offered the photostability of the previously described microglia–specific usage of DAB while making the borders of the desired anatomical region visible. MNs in the ventrolateral MN pool were counted using the optical dissector method. The results did not show any alteration in the number of MNs in the lumbar spinal cord after passive transfer from healthy volunteers compared to the untreated animals (Figure 4A, B), however, passive transfer of ALS sera resulted in a prominent MN loss (Figure 4C). The number of MNs in the lumbar segment of the spinal cord was determined by the optical disector method and expressed as number/mm^3 (Figure 4D).

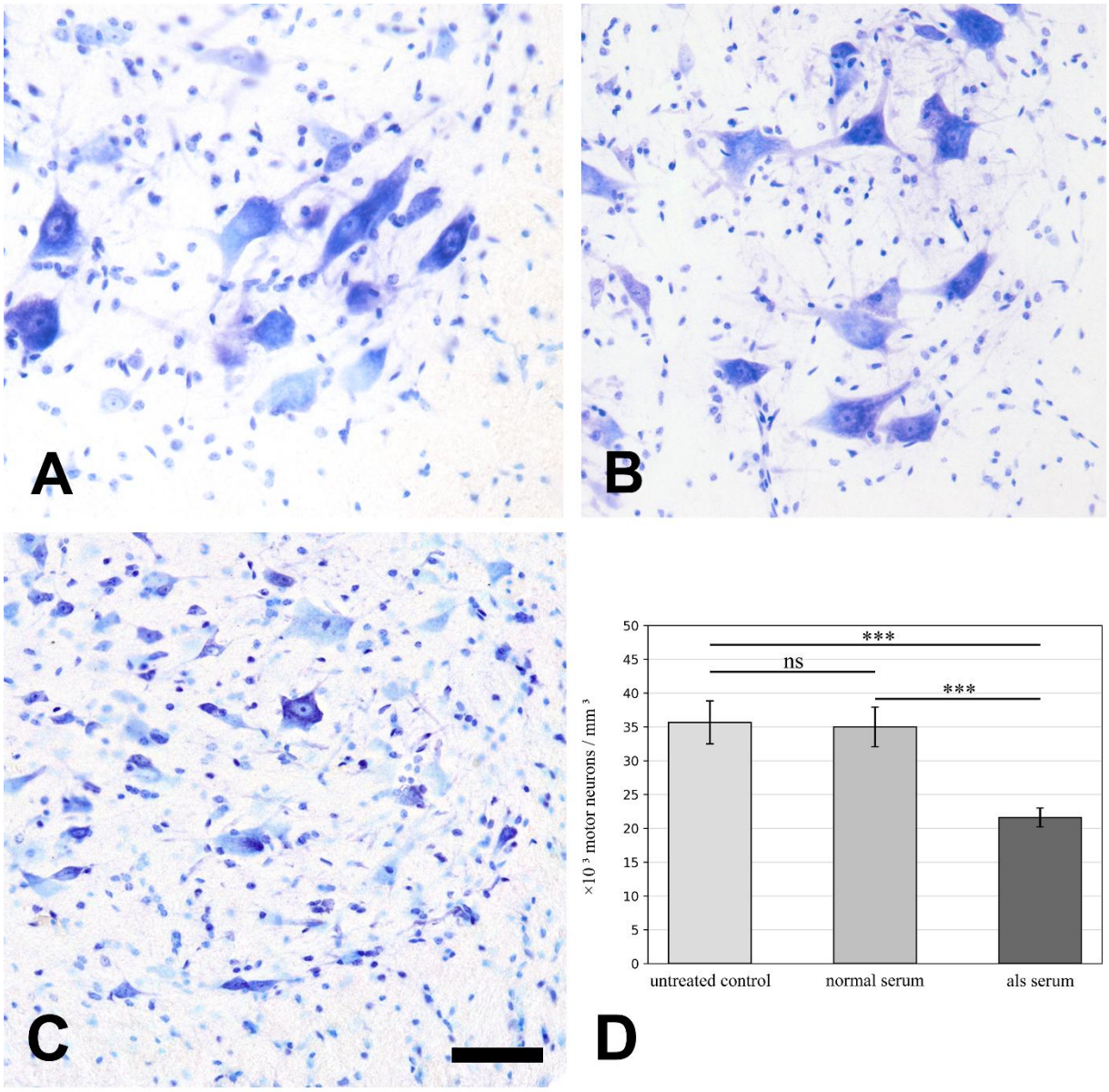

Figure 4. *Large cells (>30 µm of characteristic profile size) identified as MNs are detectable in high numbers in untreated mice (n = 3) (A) or after injection with sera from healthy individuals (n = 3) (B). A reduction in the number of MNs could be observed after treatment with serum from ALS patients (n = 14) (C). Scale bar: 100 µm. Data represented by mean value ± standard error of the mean. Statistical evaluation was determined using one-way analysis of the variance with Tukey's post-hoc comparison. ***: p<0.001; ns: non-significant.*

Changes in the calcium content of MNs after injection of ALS sera

Significant MN loss can be observed in the ventrolateral MN pool in the ALS model compared to the controls; however, subtler markers of degeneration can be noted if we investigate subcellular elements of the still-detectable cells. With electron microscopy, no ultrastructural alteration could be seen in MNs of untreated mice or after treatment with serum from healthy controls (Figure 5A, B). After inoculation with ALS sera, disorganized mitochondrial cristae, dilated endoplasmic reticulum and Golgi complexes can be observed in the perikarya of MNs compared to controls (Figure 5A-C). Increased cytoplasmic and mitochondrial calcium, visualized as a larger number of EDDs, could be observed in MNs after treatment with sera from ALS patients (Figure 5C).

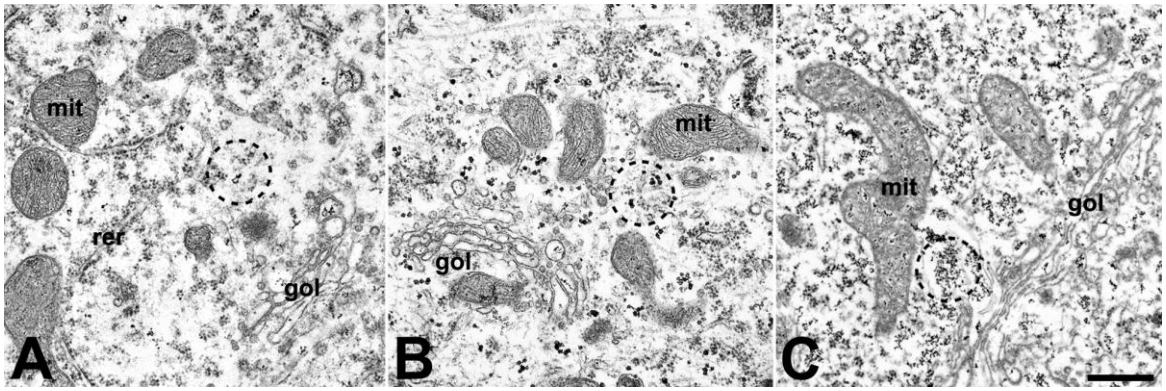

Figure 5. *No ultrastructural alterations can be seen in untreated (A) and the healthy serum-treated motor neurons (MNs) (B). The dilated lumen of the endoplasmic reticulum and mitochondrial cristae structure characterize the micrographs from mice treated with sera from amyotrophic lateral sclerosis (ALS) patients (C). In the MNs of ALS sera-treated mice (C), an elevated number of electron-dense deposits (EDDs), representing the calcium content, can be seen compared to the MNs of untreated (A) and healthy serum-treated animals (B). Dashed circles highlight EDDs. Mit: mitochondrion; rer: rough endoplasmic reticulum; gol: Golgi complex;. Scale bar: 500 nm.*

Cytoplasmic and mitochondrial calcium content was expressed as volume density of the calcium precipitates to analyze changes in the calcium levels. For such quantification, the volume occupied by EDDs was measured, then these numbers were divided with the reference volume of the cytoplasm or the mitochondrial area. Compared to controls we detected

significant increase in the calcium level induced by passive transfer in ALS serum-treated mice (Figure 6).

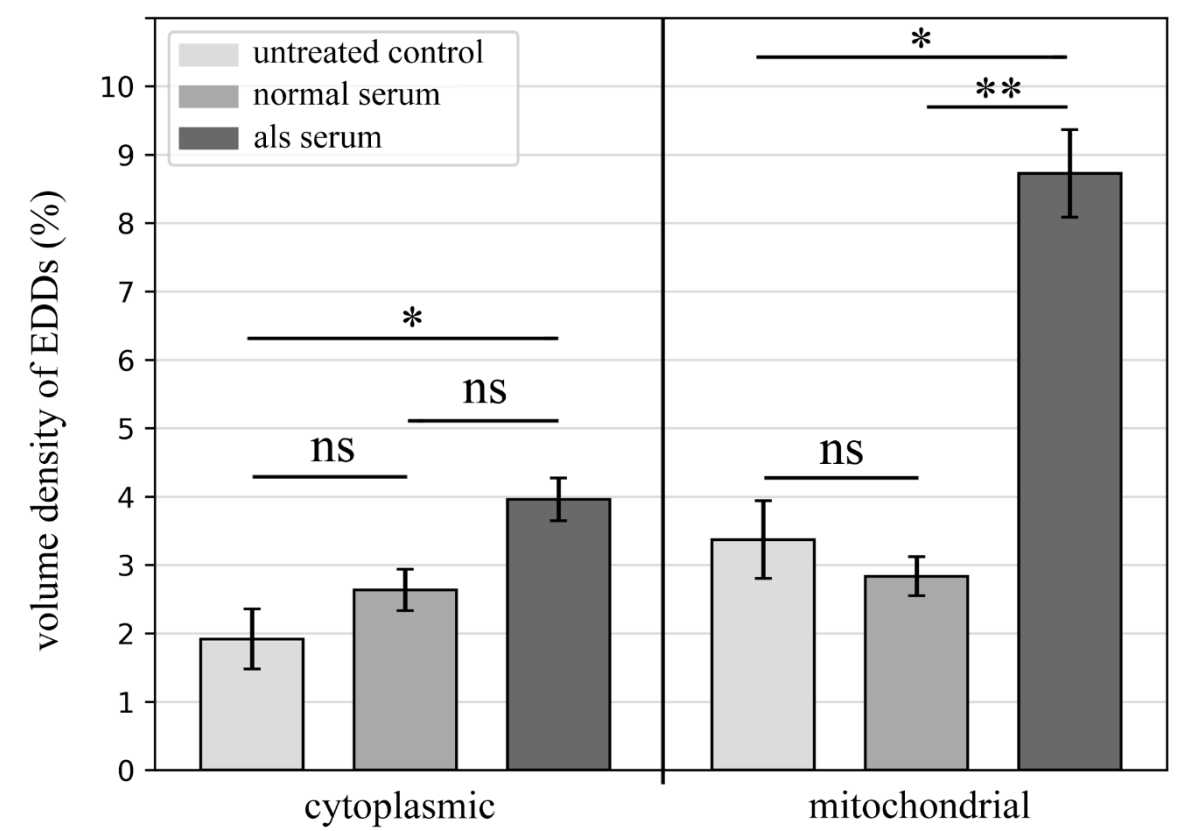

Figure 6. *A significant elevation in electron-dense deposits can be observed in cytoplasmic and mitochondrial regions of spinal motor neurons of the ALS serum-treated mice (n = 30) compared to untreated mice (n = 3) or after injection with sera from healthy individuals (n = 3). Data represented by mean value ± standard error of the mean. Statistical evaluation was determined using Kurskal-Wallis test with Dunn's multiple post-hoc comparison test. *: p<0.05; **: p<0.01; ns: non-significant.*

Correlation of intracellular calcium increase and loss of MNs

The cross-relation of the intracellular calcium level of MNs and the number of surviving lumbar MNs after passive transfer of ALS serum was analyzed by plotting these parameters after pooling the data to individual serum donor patients. Correlation analysis revealed a strong negative correlation between the number of surviving MNs and intracellular calcium level increase in the spinal cord MNs (Figure 7). The data representing the control groups (untreated and control serum-treated groups) were separated from the ALS serum-treated patients' data.

Furthermore, in the ALS serum-treated group, one subpopulation emerged; as cluster analysis separated the data representing the mice which received serum from ALS patients with a mutation in the chromosome 9 open reading frame 72 (C9ORF72) gene. This subpopulation of ALS serum-treated mice displayed more severe MN loss and highly increased intracellular calcium levels.

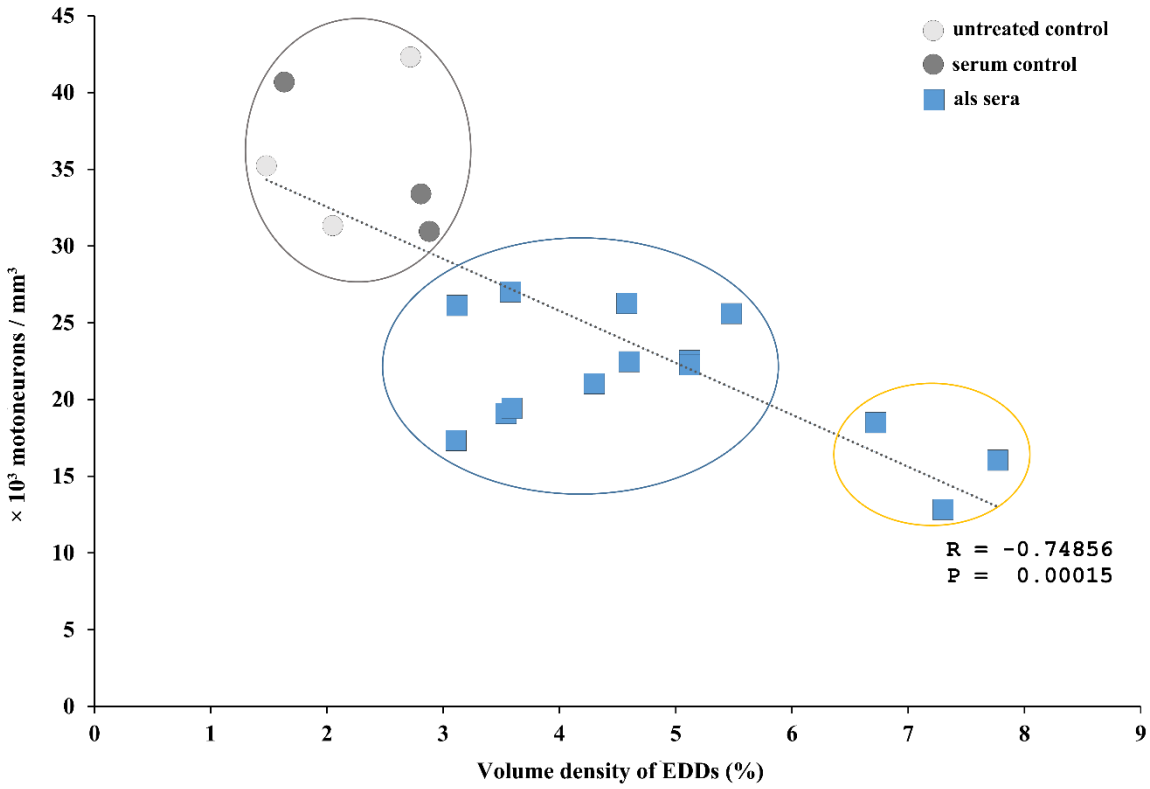

Figure 7. *On the diagram (except for the untreated animals), each symbol represents a patient who served as a serum donor. The number of surviving spinal motor neurons negatively correlated with the increase in intracellular calcium levels. Three clusters could be identified: the control groups (at the left side), the majority of the ALS patients (at the middle), and a subgroup of ALS patients with chromosome 9 open reading frame 72 hexanucleotide repeats (at the right side). Expectation–Maximization cluster analysis and Pearson correlation analysis were used for statistical evaluation.*

Effect of photobleaching on the morphometric analysis of fluorescently labeled cells

Effect on mean signal intensity

In order to determine the adequate method for a larger-scale (individual cell morphology and cell populational measurements) morphological evaluation on neurons and microglia, first, mean signal intensity was measured in large field of view images after neuronal and microglial staining using A488 and A546 fluorophores (Figure 8). Although the bleaching dynamics of the fluorophores were different, we found significant data loss as early as 30 seconds of illumination time in the case of the Iba-1 staining (Figure 9) with both conjugates. The intensity of both fluorophores was reduced by more than 10% after 60 seconds, and the intensity loss was doubled after 120 seconds of continuous illumination, regardless of the primary antibodies. At the end of the illumination series, A488 showed a 45% decrease compared to the initial intensity; furthermore, in the case of the A546 fluorophore, this intensity loss reached 65%.

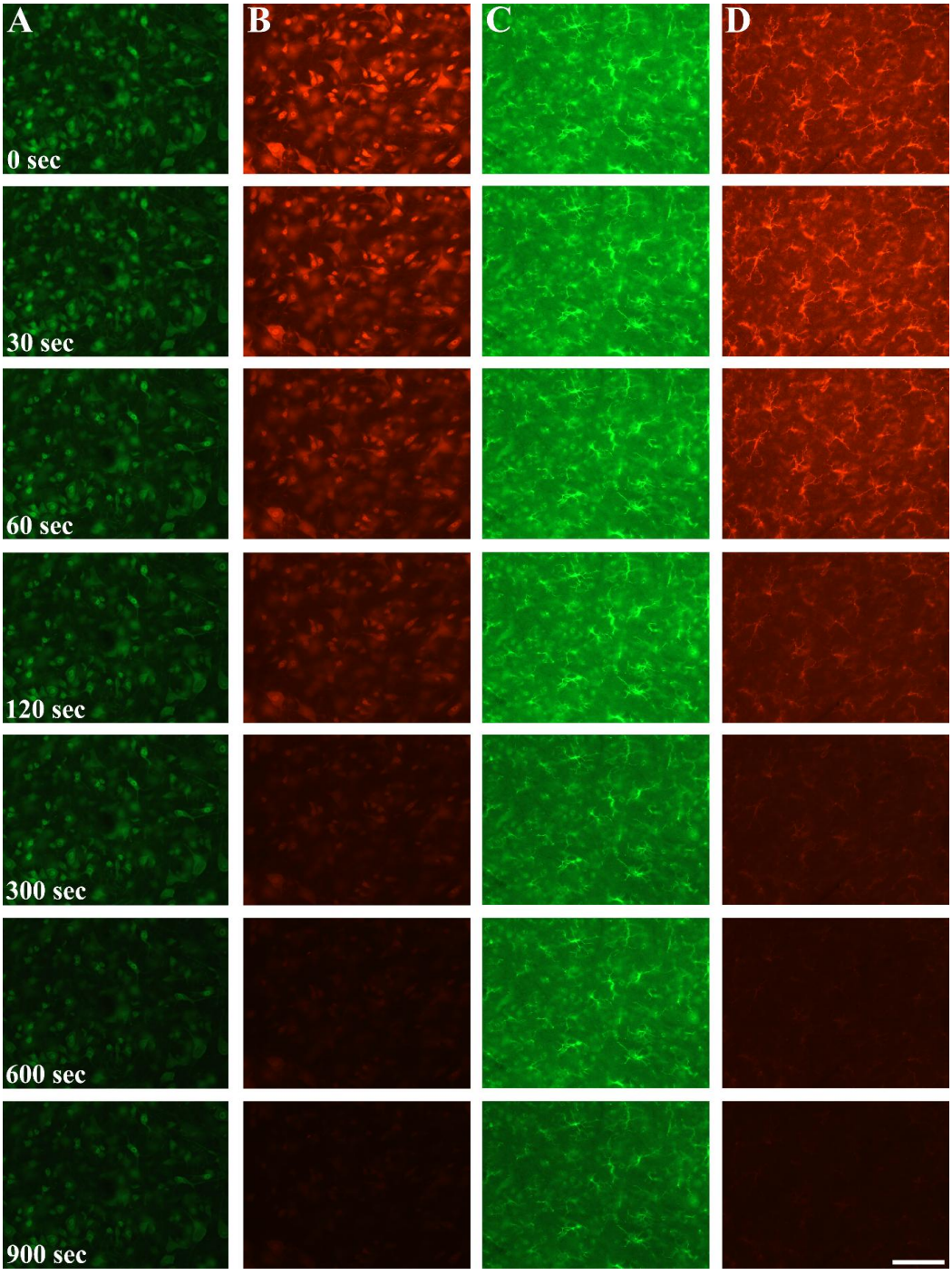

***Figure 8**. Neuronal (column A, B) and microglial (column C, D) staining using Alexa Fluor 488 Plus secondary antibody (column A, C) and Alexa Fluor 546 secondary antibody (column B, D) at 0 sec exposition, after 30, 60, 120, 300, 600 sec and 900 sec excitation times. Qualitatively, with both of the fluorophores, fading commenced as early as after 60 sec illumination time, and by 900 sec only faint staining (A488) if any visible signal (A546) is noticed. Scale bar: 100 μm.*

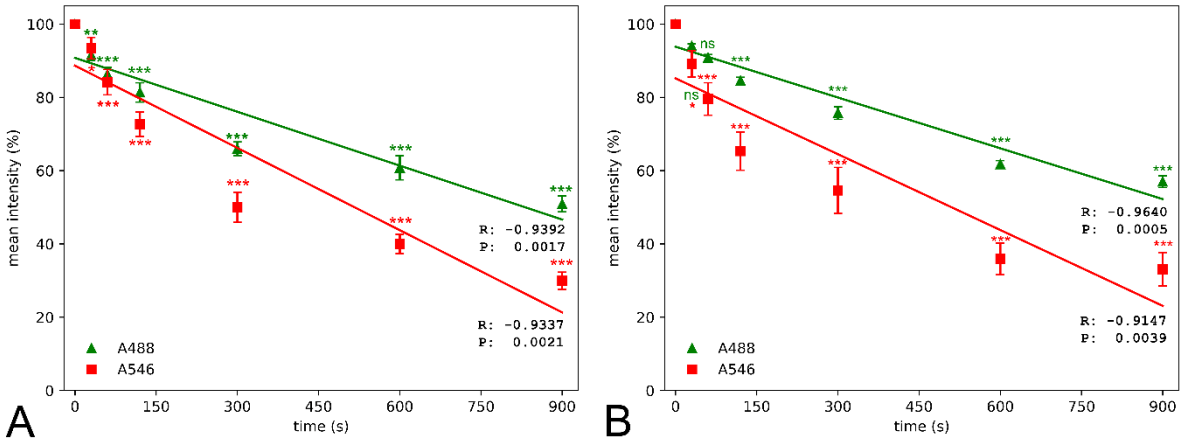

Figure 9. *Quantitative determination of mean pixel intensity revealed that photobleaching led to a significant decrease of the fluorescent light as early as after 30-60 seconds compared to values at zero illumination time (*: $p < 0.05$, **: $p < 0.01$, ***: $p < 0.001$) of microglial (A) and neuronal staining (B). A546 shows a higher mean intensity loss dynamic than A488, resulting in a significant difference ($p < 0.01$) at 90 sec illumination time and 60 sec time points in the case of microglial and neuronal staining, respectively. At later time points the level of significance is $p < 0.001$. Statistical evaluation was determined using parametric one-way analysis of the variance (A488 neuronal staining (n = 15), A546 microglial staining (n = 15)) and Kruskal-Wallis test (A546 neuronal staining (n = 15), A488 microglial staining (n = 15)) with the Dunn's multiple comparison test. This observation was confirmed by the analysis of the fitted linear regression model. ns: non-significant.*

Effect on the number of detectable neurons

Neurons in the sections were counted in the same area with different illumination times if their nuclei could still be identified. The number of detectable neuronal profiles was reduced by approximately 10% after 60 seconds of illumination of samples, regardless of the fluorophore (Figure 10). The number of neuronal profiles faded relatively slowly if samples were stained with A488 fluorophore; however, the photobleaching was more prominent in the case of A546, where the decrease in the number of NeuN-positive profiles after 120 seconds of illumination reached 20%. At the end of the experiment, A488 showed a 22% decrease in the number of detectable neurons, but more than half of the initial number of neuronal profiles became unidentifiable if samples were stained with A546.

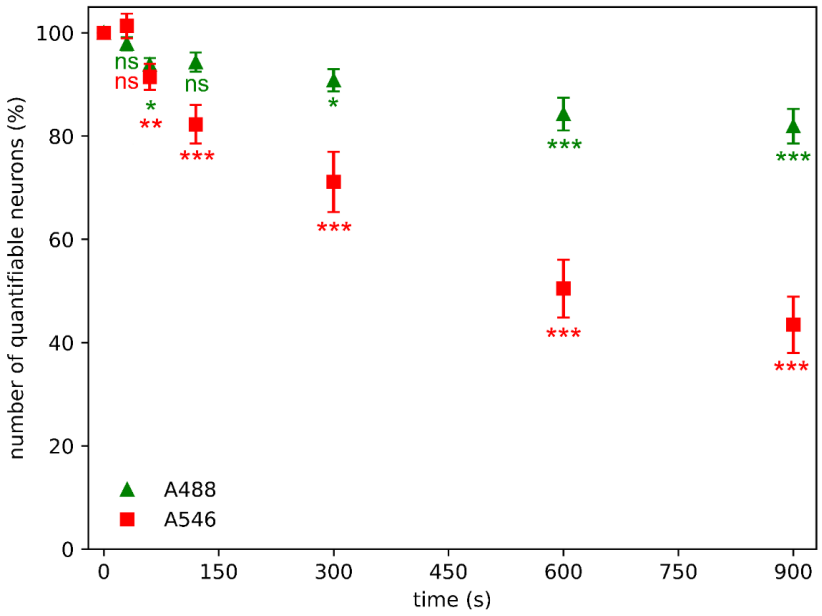

Figure 10. *Photobleaching has a significant effect on quantifiable neuronal number (stained neurons with discernible nucleus) even after 60 seconds of illumination time using Alexa Fluor 546 (A546) (n = 15) and Alexa Fluor 488 Plus (A488) (n = 15) compared to the values measured at zero sec illumination time. Statistical evaluation was determined using Kruskal-Wallis test with Dunn's multiple comparison test. *: $p < 0.05$, **: $p < 0.01$, ***: $p < 0.001$, ns: not significant.*

Effects on relative area coverage of microglial cells

The cell-to-background relative microglial profile area coverage measurement maps the background density and standard deviation of the background to provide a cut-off value of the image of interest for segmentation. Same areas at different time points were acquired, and the relative differences between the actual image and the initial image were calculated. Notable changes first occurred after 60 seconds of illumination (Figure 11); approximately 55% of alterations in the area occupied by microglia were observed regardless of the fluorophores; this change scaled up to 90% after 300 seconds of illumination.

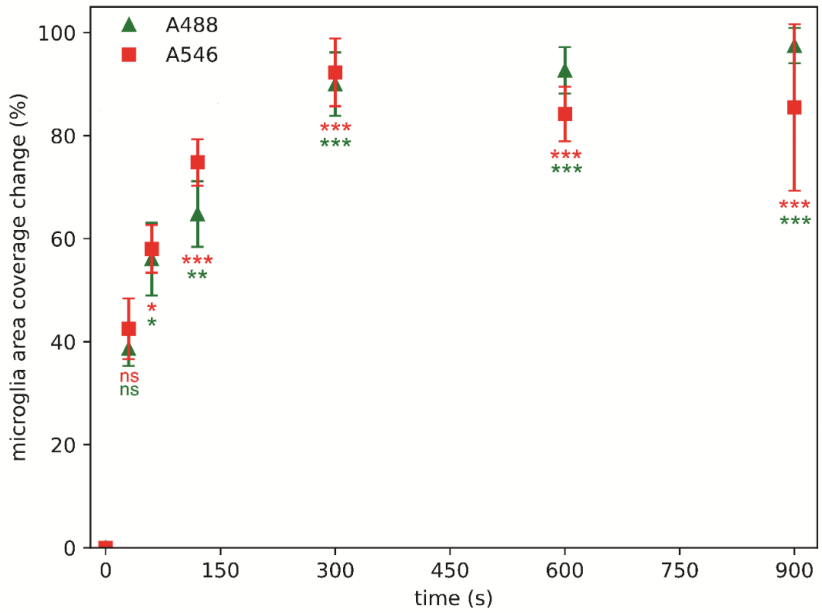

Figure 11. *Quantification of microglial area coverage alterations with the Image Pro-Plus macro. Photobleaching has a significant effect on microglial area coverage measurements even after 60 seconds of illumination time using Alexa Fluor 546 (A546) (n = 15) and Alexa Fluor 488 Plus (A488) (n = 15) compared to area coverage measured at zero time point. Statistical evaluation was determined using Kruskal-Wallis test with Dunn's multiple comparison test. *: p < 0.05, **: p < 0.01, ***: p < 0.001, ns: not significant.*

The ImageJ-based, ChatGPT-generated macro, performing image transformations, user-controlled thresholding with binarization and area fraction parameter-retrieval, was used to evaluate the images, in parallel to the Image Pro-Plus macro-based quantification. Notable changes first occurred after 30 (A488) and 120 (A546) seconds of illumination (Figure 12). The ChatGPT-generated ImageJ macro revealed similar changes as the manually-prepared Image Pro-Plus macro (Figure 11, Figure 12).

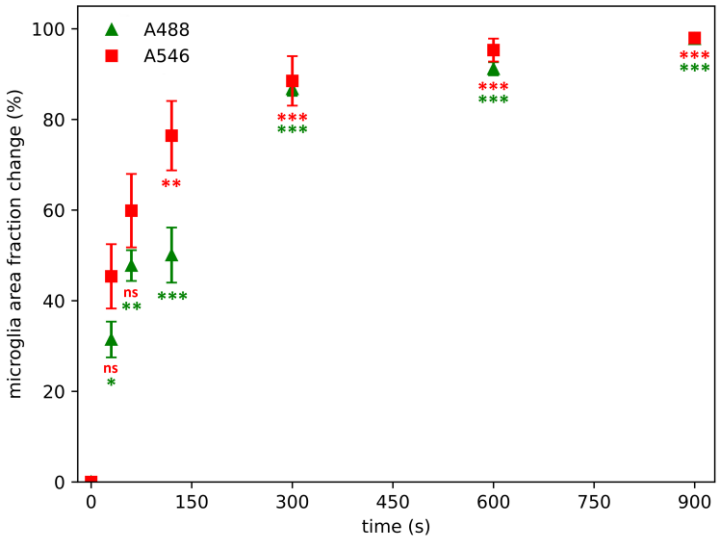

Figure 12. *Quantification of microglial area coverage alterations with the ChatGPT-generated ImageJ macro. Photobleaching has a significant effect on microglial area fraction measurements even after 30 seconds of illumination time using Alexa Fluor 488 Plus (n = 15) compared to area fraction measured at zero time point. Statistical evaluation was determined using Kruskal-Wallis test with Dunn's multiple comparison test. *: $p < 0.05$, **: $p < 0.01$, ***: $p < 0.001$, ns: not significant.*

Effects on fractal parameters of microglia cell profiles

Morphometric parameters were compared between individual cell profiles segmented from images taken at different time points (Figure 13). Based on the mean intensity changes and considering the time-consuming process of semi-manual segmentation, cell profiles were segmented at the 0-time point and at a determined endpoint of illumination time where the binarization process still could be done. This time was 120 seconds for A546 and 900 seconds for A488. The most prominent changes were observable in two of the cell-sized-based parameters (area (18% loss in the case of both conjugates) and density (15% loss in the case of A488 and 24% in the case of A546)), but the shape-based parameters also suffered significant information losses showing 4% (A488) and 6% (A546) change in fractal dimension, 9% (A488) and 15% (A546) in lacunarity, 10% (A488) and 8% (A546) in span ration, 8% (both conjugates) in perimeter and 8% (both conjugates) in circularity. Pooled fractal parameters showed 10% (A488) and 12% (A546) information change at the chosen endpoint.

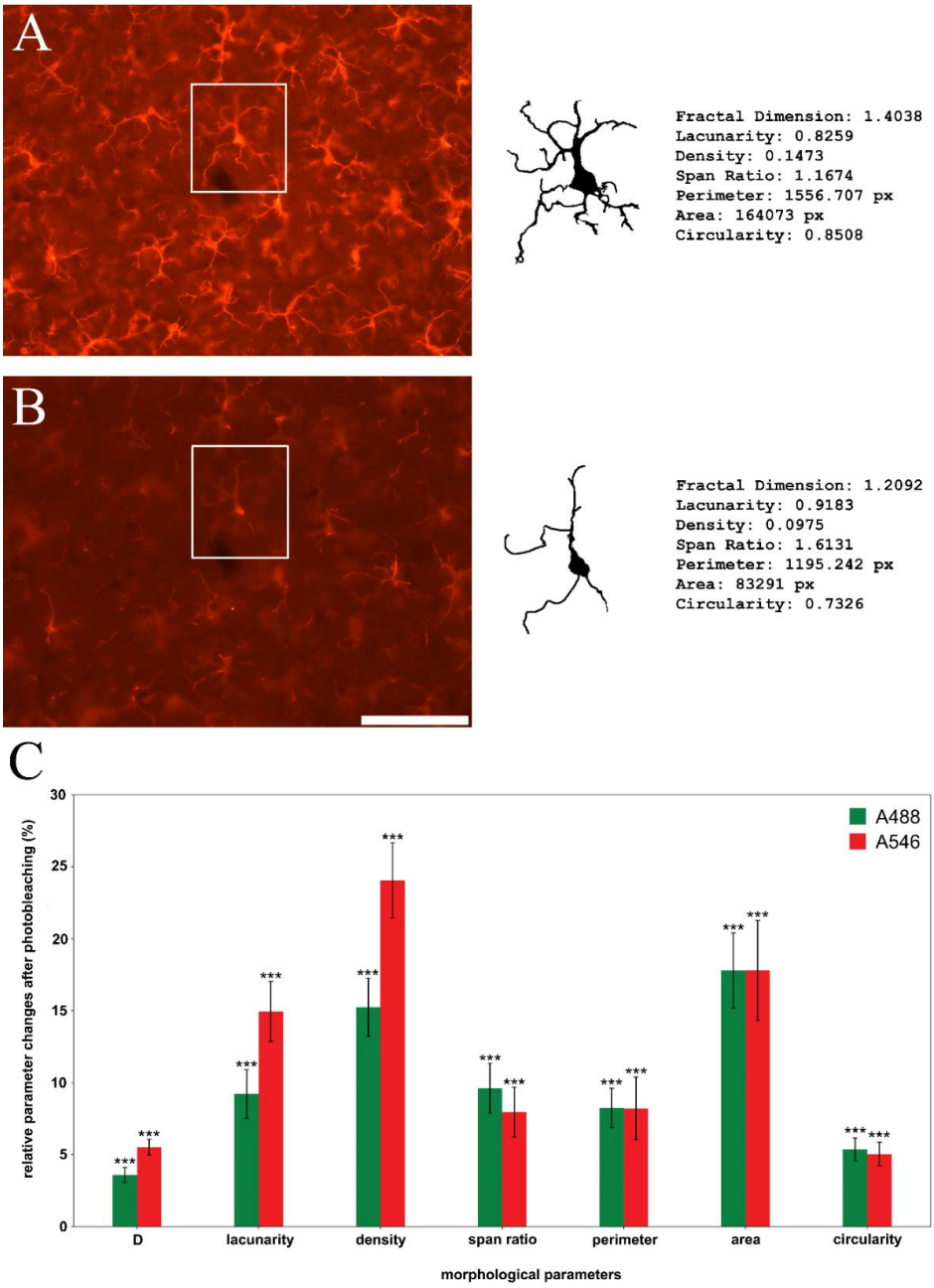

Figure 13. *Photobleaching has a significant effect on morphological parameters of individual microglial cell profiles (A: initial image, B: faded image) using Alexa Fluor 546 (A546; red bars on panel C) (n = 30) and Alexa Fluor 488 Plus (A488; green bars on panel C) (n = 30). Qualitative analysis reveals significant changes in all observed parameters (C). Statistical evaluation was performed using the one sample t-test (A546 density, A546 fractal dimension) or Wilcoxon Signed Rank Test (all other parameters) on data retrieved at the point of detection limit (900 seconds of illumination in the case of A488 and 120 seconds in the case of A546). ***: p < 0.001, ns: not significant. D: fractal dimension. Scale bar: 100 μm.*

Combination of the DAB-based and the Fluorescent-Based Immunohistochemistry

For morphological quantification within identified anatomical structure, the DAB-based and the fluorescent based immunohistochemistry in a single section were combined. For illustration purposes, sections from the hypoglossal nucleus were used, since this motor nucleus displays easily identifiable borders compared to that of the ventrolateral MNs. In Figure 14, the fluorescently stained MNs are used to identify the border of the hypoglossal nucleus, which border is then copied to the DAB-stained microglial stained image, and the microglial area coverage could be determined within this border. For illustration of the co-distribution, the two images are overlaid.

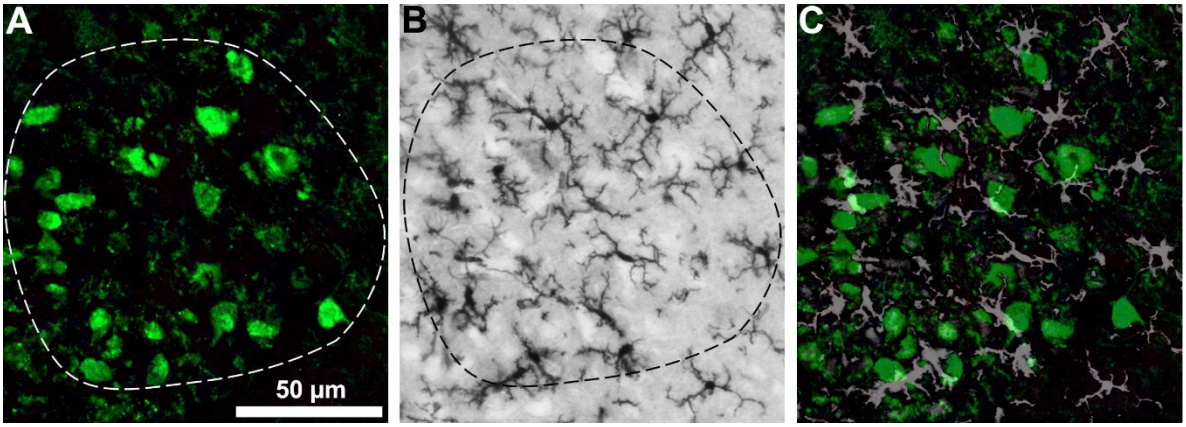

Figure 14. *Sections containing the hypoglossal nucleus were double-stained for motor neurons (MNs) (A) and microglial cells (B). The fluorescently stained (ChAT-positive) MNs are used to identify the border of the hypoglossal nucleus (A), which borderline was then copied to the image of the diaminobenzidine-based (Iba1-positive) microglial labeling (B). Finally, the microglial area coverage could be determined within this border. For illustration of the co-distribution, the two images are overlaid (C). Scale bar: 50 µm.*

Testing diagnostic potential of AI in neurological diseases

Diagnostic accuracy of ChatGPT in neurological disorders

Informatics-aided solutions have been used to evaluate morphometrical systems and disease models (see e.g. Figure 13 and [40,42]). To investigate the usefulness of informatics-aided solutions in another (clinical) field, the diagnostic efficacy of a general large language model, ChatGPT, was evaluated. When provided with a short case history of neurology-related

scenarios, ChatGPT was asked to deduce the 5 most likely diagnoses for each case. In parallel, medical doctors (MDs), and neurologist experts were also given the same cases. The most likely diagnosis provided by ChatGPT matched the true diagnosis in 68.5% ± 3.28% of the cases with CI95 of 61.74% – 74.56%, which significantly (p=0.0017) surpasses the success ratio of the MDs group (57.15% ± 2.64%; CI95: 51.91% – 62.23%) but does not reach the ratio of the expert group (81.66% ± 2.02%; CI95: 77.35% – 85.30%; p=4.54×10-4) (Figure 15). However, the five most probable diagnoses provided by ChatGPT included the correct diagnosis in 83.82% ± 2.73% with CI95 of 77.74% – 88.51% of the cases, which is nearly identical to the success rate of the expert group (p=0.996).

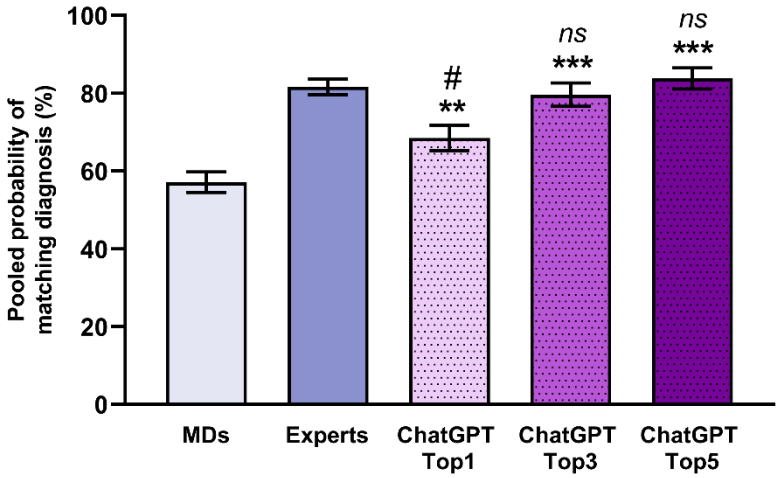

Figure 15. *Diagnostic accuracy of ChatGPT in various cases (summarized in Table 1.) where patients present with neurological symptoms. In the case of the ChatGPT group, three columns represent the most probable (ChatGPT Top1), three most probable (ChatGPT Top3), and five most probable diagnoses (ChatGPT Top5). All the data represents mean ± standard error. Pairwise comparison was analyzed with the Sidak method. **: p<0.01 (MDs vs. ChatGPT); ***: p<0.001 (MDs vs. ChatGPT); #: p<0.05 (Expert vs. ChatGPT); ns: non-significant (Experts vs. ChatGPT).*

Neurological cases were further sorted into subcategories of “acute” (n=85) and “non-acute” (n=115) cases. In the “acute cases” category, the most likely diagnosis provided by the AI matched 71.76% ± 4.88% of the original diagnoses with CI95 of 61.31% – 80.30%, which is

nearly indistinguishable (p=0.999) from the success ratio of the MDs (69.07% ± 3.47%; CI95: 61.89% – 75.44%) but slightly underachieved (p=0.013) compared to the expert group (87.99% ± 2.48%; CI95: 82.22% – 92.07%) (Figure 16A).

The "non-acute cases" subgroup represented a mixture of cases, including chronic neurological disorders, where the diagnostic procedure is often lengthy and complex, such as in the case of ALS. The diagnostic accuracy in the non-acute disease group was lower in all three groups (MDs, experts, and ChatGPT) compared to the acute neurological cases. ChatGPT achieved a diagnostic accuracy of 66.09% ± 4.41% with a CI95 of 56.98% – 74.14, based on the most probable diagnosis provided by the AI. This success ratio was similar (p=0.074) to the experts' diagnosis, which showed a success ratio of 77.35% ± 2.98% with CI95 of 71.00% – 82.65% (Figure 15B). Both groups considerably surpassed (ChatGPT Top1 vs. MDs: p=5.85×10-5; Experts vs. MDs: p=6.27×10-5) the success rate of the MDs group (48.40% ± 3.63%; CI95: 41.36% – 55.50%).

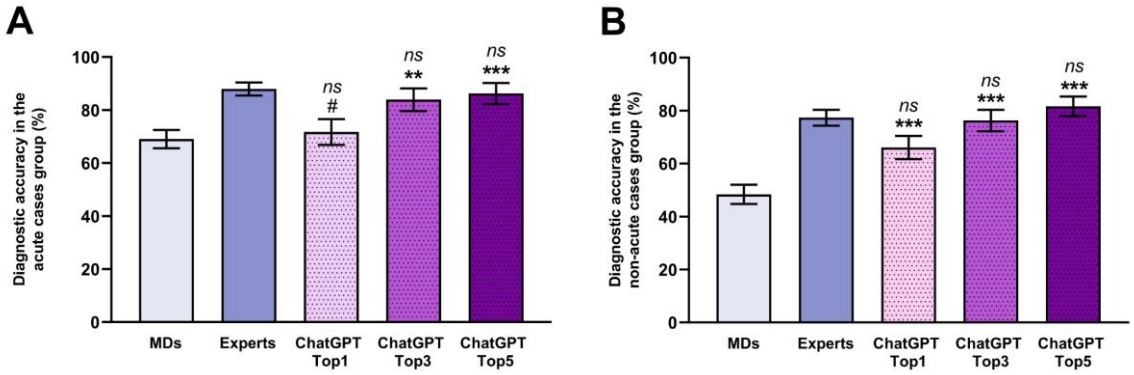

Figure 16. *Pooled success ratio of correct diagnosis for (A) acute and (B) non-acute cases (summarized in Table 1.) by medical doctors (MDs, n = 6), neurological experts (n = 6), and ChatGPT. All of the data represents mean ± standard error. Pairwise comparison was analyzed with the Sidak method. #: p<0.05 (Experts vs. ChatGPT); **: p<0.01 (MDs vs. ChatGPT); ***: p<0.001 (MDs vs. ChatGPT); ns: non-significant.*

In a few cases, all the experts failed to provide an accurate diagnosis. These exceptions were referred to as unsolved cases (n=10). Most of these cases were rare neurological disorders (e.g., spinal muscular atrophy type 4, titin-associated myasthenia gravis, antineutrophil cytoplasmic antibody vasculitis-associated mononeuritis multiplex, Pompe disease, Bickerstaff encephalitis), where the differential diagnosis is heavily reliant on further examinations and the

exclusion of alternative diagnoses. Astonishingly, the most probable diagnosis of ChatGPT matched the original diagnosis in 40% of these cases, and the five most probable AI-given answers included the correct diagnosis in 60% of the cases (Figure 17).

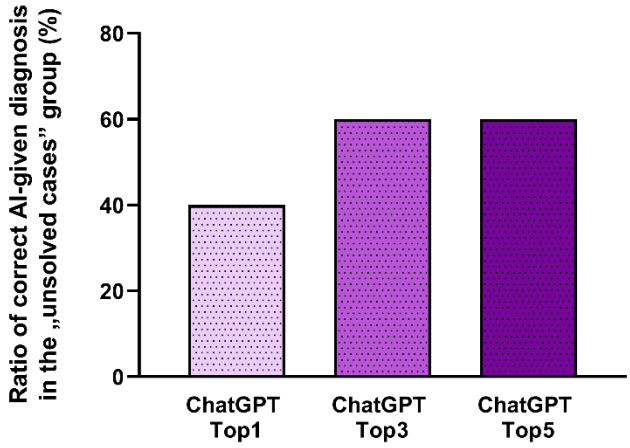

Figure 17. *All the cases where the experts have failed to provide the correct diagnosis were collected (n=10), then the success ratio of AI in these cases has been examined. The most probable diagnosis by the AI (ChatGPT Top1) was correct in 40% of the cases, and the three (ChatGPT Top3) and five (ChatGPT Top5) most likely diagnoses were accurate in 60% of the unsolved cases.*

Discussion

Common denominators in the pathomechanism of ALS

With the recent paper of Polgár et al. [43], a long story has been completed, which was initiated by the detection of IgG reactivity in the spinal cord and motor cortex of ALS patients [44]. Such observations brought into the focus of the research of pathomechanisms of ALS the immune-mediated processes [45]. Systematic studies revealed that serum of sporadic ALS patients contain antibodies to (L-type) calcium channels [46], that can induce calcium increase in a MN cell line *in vitro* [47], furthermore, can raise intracellular calcium level in cell body and axon terminals of MNs if passively transferred to mice [48]. Such *in vitro* and *in vivo* experimental data got further reinforcement from electron microscopic microanalytical data obtained from muscle biopsies from sporadic ALS patients, containing motor axon terminals, which exhibited similarly elevated intracellular calcium levels [49]. Such observation resulted in theories that in sporadic ALS the injury of MNs is based on immune-mediated processes and conveyed/initiated by antibodies enhancing the entry of calcium into MNs [50].

The focus of the research of ALS shifted towards the Mendelian familial ALS, accounting for 10-15% of the ALS patients [51], by the discovery of the first mutation associated with ALS, namely mutations in Cu/Zn superoxide dismutase (SOD1) gene [52]. By now, at least 40 genes have been identified that are associated with the disease [51]. After the first description of the SOD1 mutation, soon dozens of mutations of the SOD1 gene were identified [22] which served as a basis for developing and neuropathologically characterizing transgenic mice [53]. In such a study [54], alterations of the calcium homeostasis in the motor nerve terminals were detected, as was shown in that of sporadic ALS patients [54], and in the passive transfer model [55]. This observation raised the possibility that similar mechanisms are responsible for the degeneration of MNs in both the sporadic and familial forms of the disease.

In systematic passive transfer studies using serum from either sporadic or familial ALS patients similar motoneuronal cell loss and increased intracellular calcium could be demonstrated [29,43]. Thus, although the immune-mediated etiology of ALS is still not justified [51], the interdependent alteration of calcium homeostasis and the humoral and cellular immunological processes could be identified as at least a downstream common denominator in the chain of individual pathological episodes.

Co-detection of cellular players in ALS

As was demonstrated in our earlier studies, the dysregulation of the immune system is a key player in the pathomechanism of amyotrophic lateral sclerosis. Thus, besides the cellular victims of ALS, i.e., the MNs, their mutual localization with one of the key components of the cellular neuroinflammation, the microglial cells [56], may help in better understanding the detailed pathomechanism of the disease. For the co-localization of neuronal/motoneuronal and microglial cells, the use of fluorescent labels is the straightforward method. For this purpose, the most widely used fluorophores, Alexa fluor 546 (red) and Alexa fluor 488 (green) were selected. The limitations in the quantifications and the possibility to overcome these difficulties were investigated [57].

The problem of quantification of fluorescent signal stems from photobleaching, a well-known phenomenon; however, the extent how it affects the derived morphological data of biological samples, such as mean signal intensity, area fraction of the labeled cell compared to the background, measured arborization or fine details of the cells, etc., is less investigated. The various parameters were affected to an increasing extent in a time-dependent manner, with significant changes as early as after 30 s of illumination time. Thus, even with highly standardized settings (arc lamp intensity, detector settings, imaging features), due to the required pre-imaging adjustments (e.g., focus/z-range settings, selection of region of interest, etc.), there is an unavoidable irregularity in illumination time, consequently in the degree of fading, i.e., in derived quantitative parameters, not to mention the experienced / less experienced user-to-user variability.

To reduce photobleaching, tips and recommendations can be found on the websites of the producers of the markers; however, the issue is far from being solved. In our study, we gave an example of a combination of fluorescent and photostable visualization, which enables the fluorophore labeling of one selected cell type for localization and a DAB-based staining of another cell type for quantitative morphological evaluation. In our study we focused on the impact of photobleaching on two major cell types of the nervous system, microglial and neuronal cells, since they are widely investigated in neuronal pathology. However, the results based on the “bulky” appearance of the neurons and the “bushy”, fine structure of microglia indicate that our conclusions might also be applied to other cell types as well. Thus, the combination of photostable and fluorescent labeling might be a potential alternative to classical

multiplex fluorescent labeling, which can overcome the data-altering issue caused by photobleaching.

Machine learning in research and diagnostics

Machine learning techniques are now widely used to evaluate tissue sections in order to identify and assess the number of cellular components with minimal user interaction, which, otherwise, provides comparable detection accuracy to human field experts (see e.g., [59,60]). Thus, with a simple example, we demonstrated that image processing and repetition-automatizing macro programs can be generated using general large language models without an in-depth background in informatics or mathematics. Furthermore, we made an attempt to apply a deep learning method to identify and calculate the area coverage of the calcium-containing EDDs in electron microscopic images of ultrathin sections obtained from muscle samples and spinal cord tissue of mice devoted to passive transfer experiments. However, due to the rather irregular shape of the EDDs and the great variability of their grayscale shade, during the teaching period, we could not reach the threshold of a reliable application. Thus, instead of this automated technique, a point-counting method was applied to determine the area fraction occupied by the EDDs.

It is important to note that general large language models like ChatGPT are trained on a database with huge variety - in the case of program code writing, this means that they are going to make mistakes. The main reason for this is most of the program codes available on the internet have syntactical or semantical errors, as they were posted on forums, asking for help to correct functional errors. Based on our experience, ChatGPT is able to correct its own programming mistakes just by describing the problem, without using any programming terminology or knowledge.

Surprisingly, since the dawn of machine learning, only a few AI tools have been translated into clinical practice, possibly due to slow or complicated applications in real-life scenarios [59]. AI-based diagnostic tools can be especially useful in neurology, particularly in the case of progressively developing diseases, such as amyotrophic lateral sclerosis, where the diagnostic process is often complex and prolonged due to the necessity of the demonstration of the progressive nature of the symptoms [60].

As our results suggest, AI can be a valuable diagnosis-supporting tool in neurology, as it shows promising diagnostic capability. Using generative AIs like ChatGPT as a supportive tool can alleviate a significant burden on doctors, especially on the stretched junior MD workforce. While our results indicate an impressive diagnostic accuracy, all suggestions made by ChatGPT should further be evaluated by a medical expert to screen for potential misdiagnoses and critical diagnostic flaws. It is also noteworthy that in our experimental setup, the AI was exclusively dependent on the data (patient history and neurological examination) provided by the neurological expert. Since this data is also heavily reliant on the experience and expertise of the examiner, the currently reported diagnostic accuracy of ChatGPT only reflects the clinical scenario where the patient was already examined by a neurologist. Needless to say, the field of generative AI is changing with almost unmatched dynamics, and a specialized model trained on a bigger medical dataset can further help in overwhelmed clinical situations.

Summary

I.

It has been demonstrated that passive transfer of blood serum from ALS patients with identified mutations resulted in elevated motoneuronal calcium level and loss of motor neurons in the spinal cord of mice.

II.

It has been characterized how photobleaching alters the morphometric analysis of fluorescently labeled neurons and microglial cells, and a solution has been proposed for how this effect could be compensated.

III.

It has been demonstrated that artificial intelligence could be a valuable and precise tool in the automatization of repetitive image processing steps, and in the diagnosis of neurological diseases.

Acknowledgements

Foremost I would like to express my gratitude to my mentor and supervisors, Dr. László Siklós (Neuronal Plasticity Research Group, HUN-REN Biological Research Centre), Dr. Bernát Nógrádi (Department of Neurology, Albert Szent-Györgyi Health Centre, University of Szeged) and Dr. Roland Patai (Neuronal Plasticity Research Group) for the support and guidance through my doctoral work.

I am grateful for all the support and work of the former members of the Neuronal Plasticity Research Group, especially Dr. Árpád Párducz, Erika Bánfiné Rácz, Zalán Kádár and Dr. Valéria Meszlényi. Without their professional help, teamwork and the inspiring and friendly atmosphere they created, this dissertation would not have been possible to write.

I would like to thank the kind support and understanding of Dr. Péter Klivényi (Department of Neurology, Albert Szent-Györgyi Health Centre, University of Szeged) and Dr. Gábor Szebeni (Laboratory of Functional Genomics, HUN-REN Biological Research Centre).

I am grateful for all the members of the Department of Biophysics and Core Facilities of the HUN-REN Biological Research Centre, and the members of the Neuroscience Research Group, University of Szeged for their support, patience and understanding.

This work was financially supported by New National Excellence Program of the Ministry for Innovation and Technology of Hungary (ÚNKP-23-3 -SZTE-315), the Gedeon Richter (PhD Excellence Scholarship 2022-2024 and Short-term Research Grant 2023), and the University of Szeged (EFOP 3.6.3-VEKOP-16-2017-00009 2020 and 2021, EKÖP-24-4 - SZTE-393 2024).

References

1. von Bartheld CS, Bahney J, Herculano-Houzel S. The search for true numbers of neurons and glial cells in the human brain: A review of 150 years of cell counting. J Comp Neurol. 2016 Dec 15;524(18):3865–95.

2. Gorman AM. Neuronal cell death in neurodegenerative diseases: recurring themes around protein handling. 2008;12(6).

3. Flood DG, Coleman PD. Neuron numbers and sizes in aging brain: Comparisons of human, monkey, and rodent data. Neurobiology of Aging. 1988 Jan 1;9:453–63.

4. Guégan C, Przedborski S. Programmed cell death in amyotrophic lateral sclerosis. J Clin Invest. 2003 Jan 15;111(2):153–61.

5. Gundersen HJG. Stereology 5. Journal of Microscopy. 1981;121(1):1–1.

6. Progress in Anatomy. Cambridge University Press; 1983. 284 p.

7. Richardson DS, Guan W, Matsumoto K, Pan C, Chung K, Ertürk A, et al. TISSUE CLEARING. Nat Rev Methods Primers. 2021;1(1):84.

8. Mayhew TM, Gundersen HJ. If you assume, you can make an ass out of u and me': a decade of the disector for stereological counting of particles in 3D space. J Anat. 1996 Feb;188 (Pt 1)(Pt 1):1–15.

9. Sterio DC. The unbiased estimation of number and sizes of arbitrary particles using the disector. J Microsc. 1984 May;134(Pt 2):127–36.

10. Russ, J.C. and Dehoff, R.T., 2000, Practical Stereology, Kluwer Academic, New York, NY. - References - Scientific Research Publishing [Internet]. [cited 2025 Jul 7]. Available from: https://www.scirp.org/reference/referencespapers?referenceid=492742

11. Clarke BE, Patani R. The microglial component of amyotrophic lateral sclerosis. Brain. 2020 Dec 2;143(12):3526.

12. Franklin H, Clarke BE, Patani R. Astrocytes and microglia in neurodegenerative diseases: Lessons from human in vitro models. Prog Neurobiol. 2021 May;200:101973.

13. Appel SH, Zhao W, Beers DR, Henkel JS. The microglial-motoneuron dialogue in ALS. Acta Myol. 2011 Jun;30(1):4–8.

14. Bolognesi MM, Manzoni M, Scalia CR, Zannella S, Bosisio FM, Faretta M, et al. Multiplex Staining by Sequential Immunostaining and Antibody Removal on Routine Tissue Sections. J Histochem Cytochem. 2017 Aug;65(8):431–44.

15. Haaijman JJ. Immunofluorescence: quantitative considerations. Acta Histochem Suppl. 1988;35:77–83.

16. Bernas T, Rajwa BP, Asem EK, Robinson JP. Loss of image quality in photobleaching during microscopic imaging of fluorescent probes bound to chromatin. JBO. 2005 Nov;10(6):064015.

17. Rost FWD. Quantitative Fluorescence Microscopy. Cambridge University Press; 1991. 264 p.

18. Joseph A, Power D, Schallek J. Imaging the dynamics of individual processes of microglia in the living retina in vivo. Biomed Opt Express. 2021 Oct 1;12(10):6157–83.

19. Bennett ML, Viaene AN. What are activated and reactive glia and what is their role in neurodegeneration? Neurobiol Dis. 2021 Jan;148:105172.

20. Engel GL. The need for a new medical model: a challenge for biomedicine. Science. 1977 Apr 8;196(4286):129–36.

21. Siklós L, Engelhardt J, Harati Y, Smith RG, Joó F, Appel SH. Ultrastructural evidence for altered calcium in motor nerve terminals in amyotrophc lateral sclerosis. Annals of Neurology. 1996;39(2):203–16.

22. Dal Canto MC, Gurney ME. A low expressor line of transgenic mice carrying a mutant human Cu,Zn superoxide dismutase (SOD1) gene develops pathological changes that most closely resemble those in human amyotrophic lateral sclerosis. Acta Neuropathol. 1997 Jun;93(6):537–50.

23. Kuhnt U, Mihály A, Siklós L, Joó F. Increased retention of calcium in the dendrites of long-term potentiated CA1 neurons of the hippocampal slice. A combined electrophysiological and electron histochemical study. Histochemistry. 1988;90(3):185–93.

24. Cellura E, Spataro R, Taiello AC, La Bella V. Factors affecting the diagnostic delay in amyotrophic lateral sclerosis. Clin Neurol Neurosurg. 2012 Jul;114(6):550–4.

25. Paganoni S, Macklin EA, Lee A, Murphy A, Chang J, Zipf A, et al. Diagnostic timelines and delays in diagnosing amyotrophic lateral sclerosis (ALS). Amyotroph Lateral Scler Frontotemporal Degener. 2014 Sep;15(5–6):453–6.

26. Chieia MA, Oliveira ASB, Silva HCA, Gabbai AA. Amyotrophic lateral sclerosis: considerations on diagnostic criteria. Arq Neuropsiquiatr. 2010 Dec;68(6):837–42.

27. Brooks BR, Miller RG, Swash M, Munsat TL. El Escorial revisited: Revised criteria for the diagnosis of amyotrophic lateral sclerosis. Amyotrophic Lateral Sclerosis and Other Motor Neuron Disorders. 2000 Jan 1;1(5):293–9.

28. Brooks BR, Miller RG, Swash M, Munsat TL. El Escorial revisited: Revised criteria for the diagnosis of amyotrophic lateral sclerosis. Amyotrophic Lateral Sclerosis and Other Motor Neuron Disorders. 2000 Jan 1;1(5):293–9.

29. Obál I, Nógrádi B, Meszlényi V, Patai R, Ricken G, Kovacs GG, et al. Experimental Motor Neuron Disease Induced in Mice with Long-Term Repeated Intraperitoneal Injections of Serum from ALS Patients. Int J Mol Sci. 2019 May 25;20(10):2573.

30. Meszlényi V, Patai R, Polgár TF, Nógrádi B, Körmöczy L, Kristóf R, et al. Passive Transfer of Sera from ALS Patients with Identified Mutations Evokes an Increased Synaptic Vesicle Number and Elevation of Calcium Levels in Motor Axon Terminals, Similar to Sera from Sporadic Patients. Int J Mol Sci. 2020 Aug 3;21(15):5566.

31. Borgers M. The role of calcium in the toxicity of the myocardium. Histochem J. 1981 Sep;13(5):839–48.

32. Patai R, Paizs M, Tortarolo M, Bendotti C, Obál I, Engelhardt JI, et al. Presymptomatically applied AMPA receptor antagonist prevents calcium increase in vulnerable type of motor axon

terminals of mice modeling amyotrophic lateral sclerosis. Biochimica et Biophysica Acta (BBA) - Molecular Basis of Disease. 2017 Jul 1;1863(7):1739–48.

33. Adalbert R, Engelhardt JI, Siklós L. DL-Homocysteic acid application disrupts calcium homeostasis and induces degeneration of spinal motor neurons in vivo. Acta Neuropathol. 2002 May 1;103(5):428–36.

34. Obál I, Engelhardt JI, Siklós L. Axotomy induces contrasting changes in calcium and calcium-binding proteins in oculomotor and hypoglossal nuclei of Balb/c mice. Journal of Comparative Neurology. 2006;499(1):17–32.

35. Paizs M, Engelhardt JI, Katarova Z, Siklós L. Hypoglossal motor neurons display a reduced calcium increase after axotomy in mice with upregulated parvalbumin. Journal of Comparative Neurology. 2010;518(11):1946–61.

36. Kong J, Xu Z. Massive mitochondrial degeneration in motor neurons triggers the onset of amyotrophic lateral sclerosis in mice expressing a mutant SOD1. J Neurosci. 1998 May 1;18(9):3241–50.

37. Mayhew TM. A review of recent advances in stereology for quantifying neural structure. J Neurocytol. 1992 May 1;21(5):313–28.

38. Fritsch RS. Quantitative stereological studies on the mechanism of immuno-suppressive effect of nitrogen mustards of benzimidazole derivatives: the role of polymorphonuclear leukocytes and mononuclear phagocytes. Experimentelle Pathologie. 1979 Jan 1;17(7):446–60.

39. Domoki F, Bari F, Nagy K, Busija DW, Siklós L. Diazoxide prevents mitochondrial swelling and Ca2+ accumulation in CA1 pyramidal cells after cerebral ischemia in newborn pigs. Brain Research. 2004 Sep 3;1019(1):97–104.

40. Paizs M, Engelhardt JI, Siklós L. Quantitative assessment of relative changes of immunohistochemical staining by light microscopy in specified anatomical regions. J Microsc. 2009 Apr;234(1):103–12.

41. Fernández-Arjona M del M, Grondona JM, Granados-Durán P, Fernández-Llebrez P, López-Ávalos MD. Microglia Morphological Categorization in a Rat Model of Neuroinflammation by Hierarchical Cluster and Principal Components Analysis. Frontiers in Cellular Neuroscience. 2017 Aug 8;11:235.

42. Karperien A, Ahammer H, Jelinek H. Quantitating the subtleties of microglial morphology with fractal analysis. Frontiers in Cellular Neuroscience. 2013 Jan 30;7:3.

43. Nogradi B, Meszlenyi V, Patai R, Polgar TF, Spisak K, Kristof R, et al. Diazoxide blocks or reduces microgliosis when applied prior or subsequent to motor neuron injury in mice. Brain Research. 2020 Aug 15;1741:146875.

44. Polgár TF, Meszlényi V, Nógrádi B, Körmöczy L, Spisák K, Tripolszki K, et al. Passive transfer of blood sera from ALS patients with identified mutations results in elevated motoneuronal calcium level and loss of motor neurons in the spinal cord of mice. International Journal of Molecular Sciences. 2021 Sep;22(18).

45. Engelhardt JI, Appel SH. IgG reactivity in the spinal cord and motor cortex in amyotrophic lateral sclerosis. Arch Neurol. 1990 Nov;47(11):1210–6.

46. Appel SH, Smith RG, Alexianu M, Siklos L, Engelhardt J, Colom LV, et al. Increased intracellular calcium triggered by immune mechanisms in amyotrophic lateral sclerosis. Clin Neurosci. 1995 1996;3(6):368–74.

47. Smith RG, Hamilton S, Hofmann F, Schneider T, Nastainczyk W, Birnbaumer L, et al. Serum Antibodies to L-Type Calcium Channels in Patients with Amyotrophic Lateral Sclerosis. New England Journal of Medicine. 1992 Dec 10;327(24):1721–8.

48. Colom LV, Alexianu ME, Mosier DR, Smith RG, Appel SH. Amyotrophic lateral sclerosis immunoglobulins increase intracellular calcium in a motoneuron cell line. Exp Neurol. 1997 Aug;146(2):354–60.

49. Engelhardt JI, Siklós L, Kömüves L, Smith RG, Appel SH. Antibodies to calcium channels from ALS patients passively transferred to mice selectively increase intracellular calcium and induce ultrastructural changes in motoneurons. Synapse. 1995 Jul;20(3):185–99.

50. Siklós L, Engelhardt J, Harati Y, Smith RG, Joó F, Appel SH. Ultrastructural evidence for altered calcium in motor nerve terminals in amyotropic lateral sclerosis. Ann Neurol. 1996 Feb;39(2):203–16.

51. Appel SH, Smith RG, Le WD. Immune-mediated cell death in neurodegenerative disease. Adv Neurol. 1996;69:153–9.

52. Goutman SA, Hardiman O, Al-Chalabi A, Chió A, Savelieff MG, Kiernan MC, et al. Recent advances in the diagnosis and prognosis of amyotrophic lateral sclerosis. Lancet Neurol. 2022 May;21(5):480–93.

53. Rosen DR, Siddique T, Patterson D, Figlewicz DA, Sapp P, Hentati A, et al. Mutations in Cu/Zn superoxide dismutase gene are associated with familial amyotrophic lateral sclerosis. Nature. 1993 Mar 4;362(6415):59–62.

54. Dal Canto MC, Gurney ME. Neuropathological changes in two lines of mice carrying a transgene for mutant human Cu,Zn SOD, and in mice overexpressing wild type human SOD: a model of familial amyotrophic lateral sclerosis (FALS). Brain Res. 1995 Apr 3;676(1):25–40.

55. Siklós L, Engelhardt JI, Alexianu ME, Gurney ME, Siddique T, Appel SH. Intracellular calcium parallels motoneuron degeneration in SOD-1 mutant mice. J Neuropathol Exp Neurol. 1998 Jun;57(6):571–87.

56. Engelhardt JI, Siklos L, Appel SH. Altered calcium homeostasis and ultrastructure in motoneurons of mice caused by passively transferred anti-motoneuronal IgG. J Neuropathol Exp Neurol. 1997 Jan;56(1):21–39.

57. Beers DR, Appel SH. Immune dysregulation in amyotrophic lateral sclerosis: mechanisms and emerging therapies. Lancet Neurol. 2019 Feb;18(2):211–20.

58. Polgár TF, Spisák K, Kádár Z, Alodah N, Szebeni GJ, Klein K, et al. Photobleaching alters the morphometric analysis of fluorescently labeled neurons and microglial cells. Pathol Oncol Res. 2025;31:1612087.

59. Brasko C, Smith K, Molnar C, Farago N, Hegedus L, Balind A, et al. Intelligent image-based in situ single-cell isolation. Nat Commun. 2018 Jan 15;9(1):226.

60. Piccinini F, Balassa T, Szkalisity A, Molnar C, Paavolainen L, Kujala K, et al. Advanced Cell Classifier: User-Friendly Machine-Learning-Based Software for Discovering Phenotypes in High-Content Imaging Data. Cell Syst. 2017 Jun 28;4(6):651-655.e5.

61. Wiens J, Saria S, Sendak M, Ghassemi M, Liu VX, Doshi-Velez F, et al. Do no harm: a roadmap for responsible machine learning for health care. Nat Med. 2019 Sep;25(9):1337–40.

62. Feldman EL, Goutman SA, Petri S, Mazzini L, Savelieff MG, Shaw PJ, et al. Amyotrophic lateral sclerosis. Lancet. 2022 Oct 15;400(10360):1363–80.